Masters Thesis

Aluminum Nitride and Chromium Nitride Thin Films for Strain Gauge Application

By

Yunlong HOU

July 25th, 2010

Supervisor:
Prof. dr. P.M. Sarro
Ir. H. A. Mol (SKF)

Laboratory of Electronic Components, Technology and Materials
Delft Institute of Microsystems and Nanoelectronics
Faculty of Electrical Engineering, Mathematics and Computer Science
Delft University of Technology

Abstract

The purpose of this project was to characterize aluminum nitride and chromium nitride thin films as strain gauge materials. Thin film strain gauges have several interesting features such as low cost, compatibility with integrated circuits and possibility of application on any substrate. Thin film materials with a large piezoresistive effect are suitable candidates for strain gauges.

Low stress Al-N and Cr-N thin films of different resistivity on oxidized silicon wafer were obtained by DC reactive magnetron sputtering. Sample reproducibility and stability were studied together with the film morphology and temperature coefficient of resistance. Device fabrication processes were investigated and subsequently wafers were diced into long beams for easy deflection. After the devices were wire-bonded , the cantilever deflection method was employed to measure the sheet resistance change due to the strain.

Conductive amorphous Al-N thin films (300 nm in thickness) with electrical resistivity from $2.04m\Omega \cdot cm$ to $71.52m\Omega \cdot cm$ were sputtered and patterned. The resistance change due to temperature variance was linear and the negative TCR (temperature coefficient of resistance) can be as small as -100ppm. Nevertheless, the piezoresistive effect of conductive aluminum nitride films was very low (smaller than 2), thus they are not suitable for strain gauge application. The resistance of overstochiometric Cr-N thin films (nitrogen rich) were more sensitive to temperature change, so B-parameter equation curve fitting was adopted to describe resistance change. B parameters from 568.6 to 690.6 were founded in several samples, and the largest longitudinal gauge factor achieved is 5.21.

Given the good piezoresistive performance of Cr-N and negative TCR, the author recommends to implement compensation resistors in Cr-N thin film strain gauge applications in case of large temperature variance. Because of the isotropic piezoresistive effect in x-y plane, only when the Cr-N strain resistor is placed parallel to the object displacement direction will the gauge reach the most sensitive state to the strain.

Contents

1 Introduction

1.1 Strain Gauges Application and Classification

Strain is important in engineering because of its relation to other material properties, very important in structural analysis. Therefore, millions of strain gages are used in the field of experimental stress analysis nowadays, such as deformation monitoring of components (even as large as a building [1]), pressure data collecting in gas turbine engines blade [2] and high-pressure fuel systems, investigating crack development or strain distribution of some delicate devices and even aerospace applications. Testing newly developed components using strain gages has become a standard operation, particularly in the automotive and aerospace industry. As a result, research on strain sensors is of great relevance.

Basically, strain gauge transducers use three sensor designs: bonded metal-foil gages, diffused semiconductor strain gauges and thin films [3].

The market-dominant foil sensor consists of an insulating flexible backing which supports a metallic foil pattern. The gauge is attached to the object by a suitable adhesive. Metal foil stain gauges have been investigated for a long time, and a great variety of them is available on the market. However, due to the adhesion process, it is intrusive to the object surface. What's more, the piezoresistive effect of metal is merely due to the change of the sensor geometry, resulting in gauge factors of 2. Because of the inherent low resistivity and low gauge factor, a foil strain gauge has to be arranged in a long, thin conductive strip in a zig-zag pattern to increase the effective length, leading to less device miniaturization potential.

With the large piezoresistive effect in silicon and germanium first discovered in 1954[4], semiconductor strain gauge began to play the role of very small strain sensing elements due to the high gauge factor (the resistance of silicon changes not only due to the stress dependent change of geometry, but also due to the stress dependent resistivity of the material) and a high resistivity. Therefore, miniaturization of the sensing element turned into reality. Moreover, because of the benefits of mass produced IC fabrication technology, low cost is also possible. Nevertheless, the disadvantage of exhibiting significant temperature effects restricts the use of this design to temperatures below 120°C [5, 3]. Another little-appreciated property is that the resistance does not change linearly with strain, which makes data analysis more difficult. Silicon carbide or doped polycrystalline silicon materials can be referred to this group as well, even though temperature is not restricted as much, but repeatability in application of load cells is poor.

Thin film strain gauges have the advantage of direct deposition on the test parts. In addition, the typical thickness of the film is less than 10μm, which ensures much less disturbance to the operating environment and minimal impact on the physical characteristics of the components on which they are mounted. A number of thin film materials have several attractive properties, such as high temperature endurance, low thermal cross-sensitivity, high wear resistance and the like. Because of the compatibility with IC and/or MEMS process technology, cost of each gauge could be reduced due to miniaturization and batch processing possibility.

1.2 Challenges from SKF

1.2.1 Bearing-scale fabrication flow

This research is addressing the desire of replacing commercial foil strain gauges in SKF's ball bearing application. Expense and complicated manual steps of applying a sensor to a ball bearings let SKF look for an alternative solution by which strain gauges can be made on ball bearing directly.

To select a suitable strain gauge material, we need to understand how to make a strain gauge on ball bearings first. After discussion with researchers from SKF and a literature study [6], the proper way of fabricating sensors on bearing should be:

1. Coating a stainless steel diaphragm with an insulating layers, like PECVD oxide or spin-on glass.

2. Depositing strain sensor material onto the diaphragm with the isolation layer. Pattering it and making wire bonding pads.

3. Assembling the diaphragm to the bearing by nickel ball laser soldering.

3. Wire bonding from device pads to existing electrical connections on the bearing.

In Figure 1.1, a picture of a ball bearing as well as the sketch of the sensor is presented. In the drawing, the shiny gray areas represent the sensor structures and the pink areas the insulating layer.

Figure 1.1: Ball bearing and expected bearing-scale fabrication cross section

1.2.2 Process temperature constraint and sensor design options

During the process describe above, the fabrication temperature is a very important issue to be considered because:

- If a steel substrate is used, the maximum process temperature is limited to 600°C. A temperature higher than 600°C will change the mechanical properties of the substrate.
- Fabrication temperatures may be further limited by the thermal expansion coefficient (TEC) of steel, which is normally one order of magnitude larger than most micro-fabrication compatible materials. A non-metal film deposited at an elevated temperature causes lots of residual strain once the substrate is cooled to room temperature, resulting in a warped steel substrate. Not only is it difficult to perform lithography on the warped substrates, the deposited film with high residual stress is also prone to delaminate from the steel substrate [6]. Hence, the film is either deposited on the steel substrate at a temperature lower than 300°C or fabricated on a separate silicon wafer at high temperature and transferred to the steel substrate afterward. But the latter option[7] adds complexity and costs, which defeat the purpose of a low cost approach.

In this project, due to the contaminating nature of iron in standard IC fabrication condition, silicon wafers were used as the test substrate. But during the process selection, temperature constraints originating from the use of steel substrate should be considered.

Since the high-temperature deposition and annealing temperature is usually one of the keys in obtaining a high quality semiconductor film, such as polysilicon, the temperature limitation imposes a significant constraint on film choice. Because of this, semiconductor strain gauges are not an option.

Consequently, IC compatible (mass production) low fabrication temperature thin film strain sensor have to be explored as a suitable option for SKF.

1.2.3 Sensor requirements

SKF is interested in making low price strain sensors which should be mass producible on ball bearing. Meanwhile, the sensor should meet the following electrical and mechanical requirements (see Table 1.1).

Table 1.1: Requirements of strain sensor materials proposed by SKF

Working temperature	-40°~125°C
Maximum fabrication temperature	600°C
Gauge factor	>2
Resistance	$>1k\Omega$/resistor[a]
Resistor shape	Square is preferred.
Thermal Expansion Coefficient (TEC)	6~15 ppm/°C[b]
Temperature Coefficient of Resistivity	The lower, the better.
Residual stress of the film	Lower stress films are preferable.

[a] In IC technology, thin layer often means the thickness is less than $1\mu m$. Referring many thin film materials studies[1~9], the sputtered thickness is often in the range of 300nm to 700nm, so the corresponding resistivity of the material should be about $30m\Omega \cdot cm$ if the resistor is square-shaped (which is preferable by SKF).

[b] TEC should be in the range of ±30% of the steel (11.5 ppm/°C). What's should be noticed is in between steel diaphragm and sensor layer SOG exists. TEC of glass various from 3.2 to 9.4ppm/°C, so the lower limit of TEC can be around 6ppm/°C.

The identification of a suitable material and its characterizations are the main objects of this project.

1.3 Thesis Organization

Introductions about strain gauge applications and SKF's requirements are given in Chapter 1. Thin film solutions were found during the discussion in this chapter. Chapter 2 reviews many possible candidates for thin film strain gauges and describes how the most promising ones are selected. In addition widely used methods to characterizing strain gauge materials are described.

Chapter 3 and 4 focus on the fabrication and on-chip characterization of thin aluminum nitride and chromium nitride layers, respectively. Resistivity, intrinsic stress and TCR of the layer deposited at various conditions can be found these chapters as well. In Chapter 5, the device layout design, PCB design, dicing and wire bonding, and gauge factor characterization are presented. The analysis of gauge factor measurement results is reported at the end of this chapter.

The thesis ends with conclusions and recommendations for future work in Chapter 6 and additional results are reported in the appendixes.

2 Thin Film Piezoresistive Materials

An electrical-resistance strain gauge operates on the principle that the electrical resistance or conductance changes when there is elastically deformation due to an applied stress. In Section 2.1, one dimensional strain piezoresistive effect is briefly discussed. A list of interesting thin film strain gauge materials is illustrated in Section 2.2, and finally aluminum nitride and chromium nitride are selected as materials for our study. Section 2.3 reviews important parameters to be discussed during the material characterization. At the same time, methods of testing the material properties are also included in this section.

2.1 Strain and Piezoresistive Effect

When a force F is applied on either end of a one-dimensional line, the length of the line can be elongated from l_0 to l_x(Figure). The relative elongation is defined as the strain ε_{xx} in this one-dimensional material:

$$\varepsilon_{xx} = \frac{l_x - l_0}{l_0} = \frac{\Delta u}{\Delta x}$$

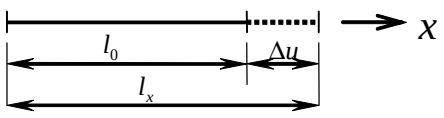

Figure 2.1: Deformation of 1D material (Δu is the displacement in x direction)

For a multidimensional case, more components of strains should be defined in terms of the displacement field[8].

Resistivity of some material will change when the object is under strain and this phenomenon is defined as piezoresistive effect. For single crystalline silicon, energy band theory can be adopted to explain the piezoresistive effect [4] and a piezoresistive tensor can be calculated. Good theoretical explanations are not fully developed for other materials.

2.2 Material selection

A table summarizing thin film materials that could be used for strain gauges and their deposition methods is given in Table 2.1.

It can be seen from Table 2.1 that most researchers used reactive sputtering technique to get compound layers because of the production flexibility. Considering both

Table 2.1: Review of feasible thin film strain gauge candidates

Gauge Material	Gauge Factor	Resistivity ($m\Omega \cdot cm$)	TCR(ppm/°C)	TEC(ppm/°C)	Sample fabrication method	References
AlN	3.72 to 15	1 to 500000	-1281 to 825	6.2	RF or DC reactive sputtering	[9]
TiN	–	0.025 to 0.031	588	9.4[10]	Hollow cathode discharge	[11]
CrN	6 to 18	0.5 to 3.8	-800 to -180	7.16[12] to 11.29	DC reactive magnetron sputtering	[13]
CrN/TiAlN	3.5	–	–	–	Cathodic arc evaporation	[14, 15]
Cr-O-X	5.2 to 10.3	–	-50 to 50	–	Magnetron co-sputtering	[16]
Ta-N	3.41 to 6.24	0.3to 3.39	-361 to -36	3.6	DC reactive magnetron sputtering	[17]
TaN-Cu	2.33 to 5.06	–	-800 to 200	3.6	DC reactive co-sputtering	[18]
TaON	2.5 to 3.5	0.27 to 2.8	-2200 to -290	–	RF reactive sputtering	[19]
WSi2	2.0 to 2.2	0.288	-450	9.2 to 13.7	DC magnetron sputtering	[20]
ITO-Al	2.1 to 7.98	–	1200	–	RF reactive sputtering	[21]

layer properties and target availability, aluminum nitride and chromium nitride layer appear to be potential candidates. Because of the Aviza Sigma 204 sputtering system available in DIMES only provides DC/pulse DC power, for the materials in this project RF sputtering is not used[1].

2.3 Material Characterization Methods

The objective of this section is to provide fundamental indicators commonly used to characterize piezoresistive materials. This section is in no way intended to specify every measuring tools used in this project. Instead, the focus of this section is on (1) identifying the parameters commonly used to qualify a material, and (2) identifying basic philosophy of measurement of some equipment.

2.3.1 Electrical Resistivity and Resistance measurement

Electrical resistivity is a primary quantity that should be obtained during characterization of a piezoresistive material. Sheet resistance and thickness of the film can be measured directly and resistivity can be acquired by a simple calculation.

2.3.1.1 Sheet resistance at room temperature

The resistance of a uniform block is given by $R = \rho L/A$ in which ρ is the resistivity of the sample, L is the length in the current direction and A is its area of the cross-section perpendicular to the current flow. "A" is the product of the width and height of the block. If we divide the resistivity with the thickness "D", the resistance can be expressed as $R = (\rho/D)\,(L/W) = R_{\square}\,(L/W)$. Once the resistance "$R$" and the geometry factor "L/W" are known, we can deduce resistivity of the material from $R_{\square}$.

Sheet resistance can be measured relatively easily and inexpensively by CDE ResMap Machine which is a powerful process monitoring tool combined with wafer mapping. Four collinear probes with equal spacing "S" as illustrated in Figure 2.2 are used. A DC current is driven passing through the outer two probes and voltage is measured across the inner two probes. If the depth of the thin film is much smaller than the space of between needles, the resistivity is given by equation $\rho = (\pi D/\ln 2)\Delta V/I$ and its unit is $[\Omega \cdot m]$. As a result, we can calculate the sheet resistance as: $R_{\square} = \rho/D = (\pi/\ln 2)\,\Delta V/I \approx 4.53\Delta V/I$.

2.3.1.2 Sheet resistance at elevated temperature

The above method can only be carried out at room temperature. A temperature control module is not available in the used equipment. In order to measure the resistance at a certain temperature, the substrate of the sample should be heated or cooled during which resistance measurement is performed. In practice, Agilent parameter analyzer, Cascade probe station combined with a TEMPTRONIC thermal inducing systems is used together and a specific measurement structure needs to be fabricated on the thin film sample (see Figure 2.3).

[1] RF reactive sputtering is necessary for insulating target because it is the only way of maintaining plasma.The use RF power to sputter conductive target leads to a slow deposition rate but a more uniform or high quality layer.

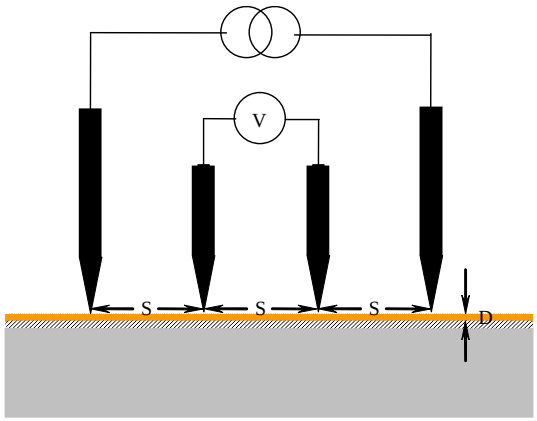

Figure 2.2: Four-point probe measurement

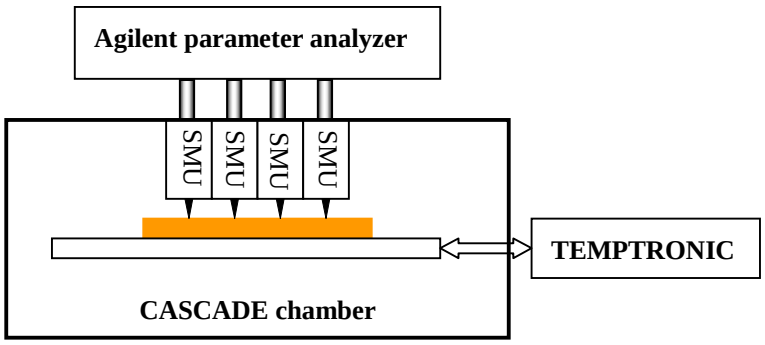

Figure 2.3: Schematic of the resistance measurement set-up at elevated temperature

VanderPauw geometry [22] is used a lot in semiconductor fabrication to monitor the on chip resistance or hall effect of different layers. There are four terminals in this structure. Forcing current through two adjacent terminals, a voltage drop can be obtained over the other two. If the structure is symmetric, the sheet resistance of the film can also be calculated as $R_{\square} \approx 4.53 \Delta V/I$[22]. An example of a VanderPauw structure (Greek cross) which is widely used is shown in Figure 2.4.

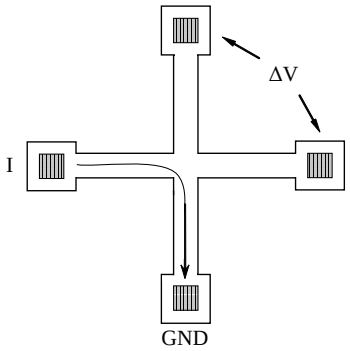

Figure 2.4: Greek cross VanderPauw structure

2.3.2 Thin Film Stress

After the film deposition and/or planarization process, residual stresses are generated and remain in the material when external stress is removed. These stresses add

themselves vectorially to the stresses caused by external forces[23]. If large residual stresses exist in thin films, a small strain will cause failure or will break the film.

Many authors adopted the curvature method to measure thin film stress [24, 25]. If material properties of the films and substrates are known, the stress of the deposited thin film layer can be calculated from the Stoney's equation:

$$\sigma = \frac{E_s}{6\,(1-\nu_s)}\frac{t_s^2}{t_f}\left(\frac{1}{R_{post}} - \frac{1}{R_{pre}}\right)$$

where E_s and ν_s are Young's modulus and the Poisson coefficient of the substrate, thickness of the substrate and the film are t_s and t_f, respectively. The parameterR_{pre} and R_{post} are the radius of curvature before and after thin film coating (See Fig 2.5). If the substrate is (100) silicon wafer, $E_s/\left[6\,(1-\nu_s)\right] = 1.805 \times 10^{11} N/m$.

In DIMES, the radius measurement of the wafer is performed on a TENCOR FLX-2900 system. A laser beam is incident on the surface of the film. The reflected light provides the radius information. The thickness of the layer is measured by using a profilometer (DEKTAK8). A negative value of σ indicates compressive stress and a positive value indicates tensile stress.

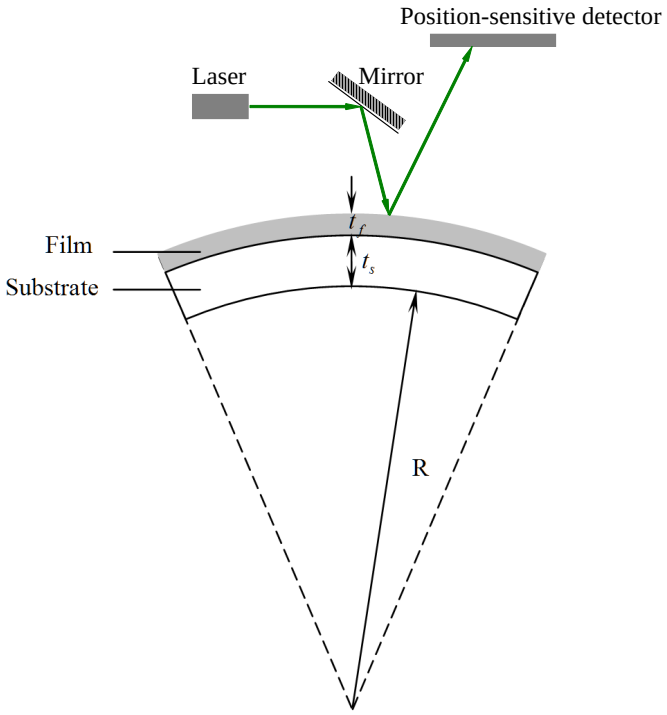

Figure 2.5: Schematic illustration of the scanning laser method for measuring substrate curvature (not to scale)

2.3.3 Temperature Influence on Resistance

Generally the resistance of a material varies with temperature. Some materials resistance will increase with the temperature, while for others will decrease. In most cases, metals have a positive temperature coefficient, while semiconductors have a negative one.

2.3.3.1 Resistance change with temperature

When an electric field is applied to the metal conductor, "free electrons" drift from one end to the other. Electrons scattering caused by the thermal motion of the metal ions limit the speed of the electron flow. This is the primary source of resistance in metal[2]. A higher temperature enables more severe thermal vibration of the metal ions, and consequently of the scattering effect, resulting in a positive temperature coefficient of resistance.

The conduction in intrinsic semiconductor is from thermal excitation. When the temperature is higher than 0K, some valence electrons are excited to the conduction band where electrons can move against the electric field. As the distribution of occupied state in the valence and conduction bands is Boltzmann distributed, the number of intrinsic carrier increases significantly[3] with the temperature which lead to a sharp drop in the resistivity.

If the semiconductor is doped, the main contribution of the carrier is from the dopant atoms. The number of the carrier is many orders of magnitudes higher than intrinsic semiconductor and it is basically stable[4]. Take n-type silicon for example, the resistivity is related to the mobility of the carrier and the number of the carrier $\rho = \frac{1}{qn\mu_n}$. Carriers mobility is confined by two factors - lattice scattering and impurity scattering[5]. If silicon is highly doped, the resistivity will decline with the temperature first and then increase due to the lattice scattering [27].

2.3.3.2 TCR and B parameter equation

In a narrow range of thermal variance, the temperature influence on resistance can be treated as linear: $R(T) = R_0\left[1 + \alpha_{tcr}(T - T_0)\right]$ where T_0 is room temperature and the α_{tcr} is the TCR value . The unit of TCR is usually parts per million per degree, which is often abbreviated as "ppm/$^\circ C$". For instance an aluminum layer has TCR of $+3900\text{ppm}/^\circ C$.

However, using α_{tcr} to describe the resistance sensitivity to the ambient temperature is not very precise. If the first linear approximation doesn't stand, a more accurate formula to predict the change of the resistance should be employed. Steinhart-Hart equation[6] is a good model of the resistance at different temperatures. B parameter equation[7] $R = R_0 \exp[B\left(\frac{1}{T} - \frac{1}{T_0}\right)]$ also stands for resistor with negative temperature coefficient[28] which is essentially the Steinhart-Hart equation with c = 0 and B = 1/b.

2.3.3.3 Importance of TCR

Temperature plays a role in strain measurement that can't be neglected because of non-zero TCR. When the ambient temperature changes, output of the strain gauge will not be reliable due to the change in resistance $\left(\frac{\Delta R}{R}\right)_{\Delta T}$. In addition, the mismatch of the substrate TEC (β) and the gauge material TEC(α) will also induce resistance change during temperature cycle. The resistance change due to temperature can thus be expressed as

[2] Discontinues of electrical potential results from lattice imperfection is a minor source in metals

[3] $n_0 = p_0 = 2\left(\frac{2\pi m_p^\star kT}{h^2}\right)^{3/2} exp\left[\frac{-(E_F - E_v)}{kT}\right]$[26]

[4] If the temperature is higher enough, the dopant atoms will diffuse

[5] $\mu_L \propto T^{-\frac{3}{2}}$, $\mu_I \propto T^{\frac{3}{2}}$

[6] $\frac{1}{T} = a + b\ln(R) + c[\ln(R)]^3$

[7] Standard relative error of B-parameter equation is 0.06012

$$\left(\frac{\Delta R}{R}\right)_{\Delta T} = (\beta - \alpha) \cdot GF \cdot \Delta T + TCR \cdot \Delta T$$

In order to reduce the effect of unstable ambient temperature, TCR and ΔTEC should be kept as low as possible. So TCR is an importance parameter that should be measured during the material characterization. The measurement system prepared as in Figure 2.3 was used to monitor the temperature influence on resistance. The accuracy of the temperature can reach +/-0.1°C and the cycle of the temperature is between -20°C and 100°C.

2.3.3.4 Non-zero TCR adjustment

A material with large TCR can be adjusted by integrating thin film temperature sensor onto the strain gauge area. Pt [29] and Ni [6] thermal resistors are examples of this solution. In addition, Wang's study indicates implanting dopant atoms like copper as a helpful way to compensate TCR of TaN [18].

2.3.4 Gauge Sensitivity and Gauge Factor

The sensitivity of a piezoresistive sensor is quantified as gauge factor which is defined as the percentage change in resistance per unit strain, or in equation as $GF = (\Delta R/R)/\varepsilon$.

2.3.4.1 Methods of measurement

The value of gauge factor is obtained by monitoring the resistance variance while the resistor is strained. Different ideas of recording the strain require other set-ups for gauge factor measurement. These recording methods are described in detail in this section.

- The cantilever deflection method [30] is mostly adopted and the strain information is recorded from the force applied to the tip of the cantilever [31, 14] (see Figure 2.6).

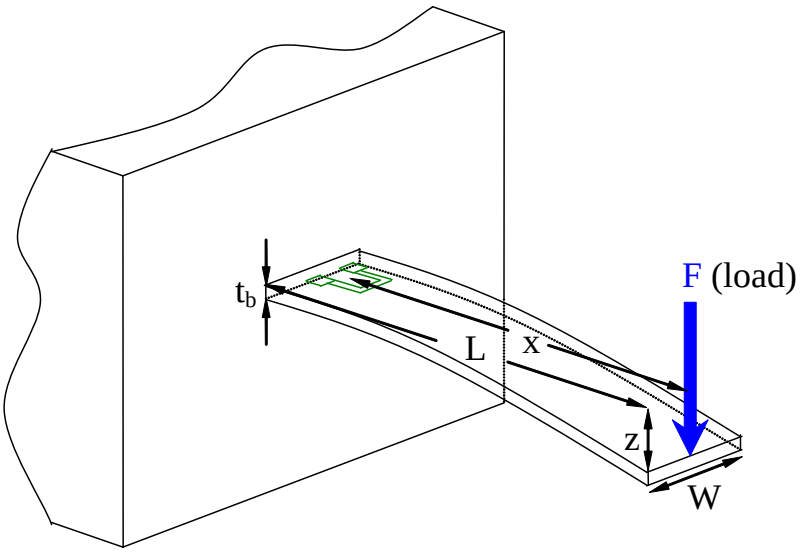

Figure 2.6: A cantilever under deflection

Gauge factors are calculated from the change in electrical resistance in response to a longitudinal strain $\varepsilon = 6Fx/(EWt_b^2)$, where E is Young's modulus of the beam, W is the beam width, t_b is the beam thickness and x is the distance from the center of the gauge to the point of application of the load F.

- Another way of computing the strain is by introducing the moment of inertia to cancel out the Young's modulus and load F. The formula changes into $\varepsilon = 3xzt_b/(2L^3)$. However, the displacement of the tip z should be known [32].

  LVDT(Linearly variable differential transformer) extensometer is commonly used to record the tip displacement [33]. It has one primary wire coil, two secondary wire coils and one magnetic core which can move in between. When the metallic core is moved from the zero position, the voltage in the secondary coils becomes unbalanced and an electronic signal is induced in the leads.

- The deflection of the beam can also be adjusted via a microscrew, which is directly readable. In Creemer's thesis [34], a test equipment was designed and the beam under test was deformed to an accurate value through a microscrew.

  This set-up is adopted in this project to test the gauge factor. The piezoresistor on the beam is connected to the coaxial/triaxial connector via a set of PCB and a DIN 41612 connector. The complete schematic topview diagram of this measurement system is drawn in Figure 2.7(a). This design also provided the possibility of differential measurement, which means two identical beams can be installed into this equipment, with one beam deflected while the other is in its original position.

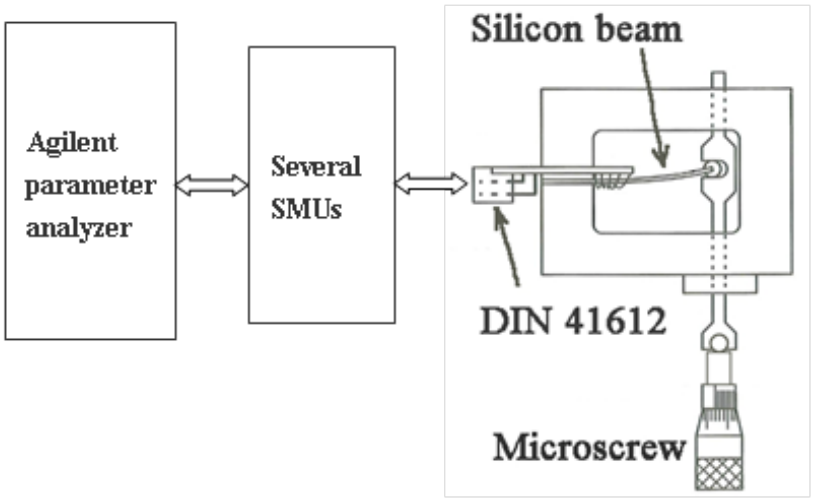

(a) Schematic diagram of gauge factor testing system.

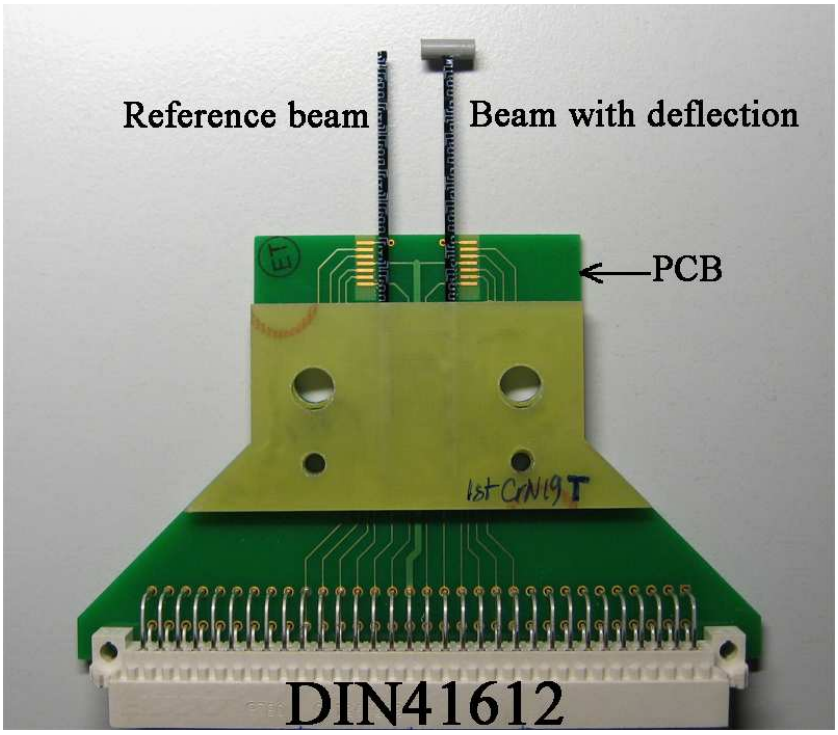

(b) Differential test beams clamped with PCB. The beam with a small cylinder will be deflected in the test.

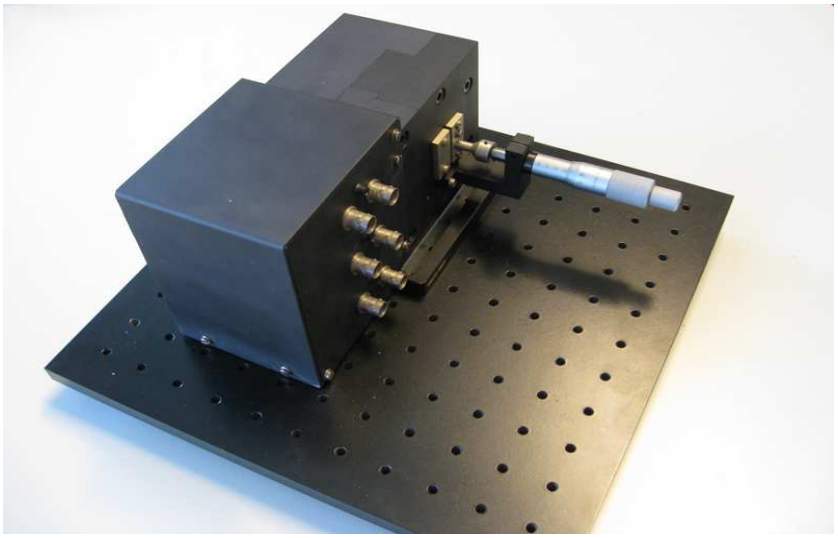

(c) Equipment designed by Creemer, corresponding to (a) without connecting to parameter analyzer.

Figure 2.7: Gauge factor measurement setup.

The methods of testing the performance of a strain gauge are not restricted to the above ones. In reference [35], [36] and [37], other test structures were proposed and were all acceptable alternatives.

3 Thin Film Aluminum Nitride

3.1 Sample Preparation

Aluminum nitride thin films can be prepared by reactive sputtering process. Some researches focus on growing Al-N in wurtzite structure preferentially with c-axis orientation to get good piezoelectric properties. Electrical insulation is also one of known property of piezoelectric materials. So it is impossible to use crystallized aluminum nitride as a strain gauge candidate. Aluminum nitride films sputtered on glass substrate in DC triode system with different resistance values were reported in Vacandio's research [38]. Tuning gas flow can change the resistivity of the deposited film.

3.1.1 Film Deposition

The recipe to sputter aluminum nitride was designed based the ones used for pure aluminum layers and dielectric AlN layers. As the nitrogen percentage increases from 0% to 100%, the film will change from pure Al metal to highly crystallized Al-N films. The total reaction gas pressure should be lower than 1 Pa (=7.5mTorr), otherwise the surface edge/center deposition ratio (uniformity) becomes worse for Al, Cu and Mo sputtering [39]. So the total gas flow (Ar and N2) during the sputtering was set to 56sccm (2.2mT). The sputtering power, bias, temperature and time were set to 2kW, 0W, 300°C and 300s as starting point.

Table 3.1: Sputtering recipes for conductive aluminum nitride selection

Sample No.	Ar (sccm)	N_2 (sccm)	Thickness (nm)	Deposition rate ($\mathring{A}/(kW \cdot s)$)	$R_\square$ ($\Omega/\square$)	Resistivity ($m\Omega \cdot cm$)
1	53	3	1080	36	0.0276 ±0.00024	0.00298
2	48	8	633	21.1	0.0903 ±0.0016	0.0057
3	42	14	1189	39.6	0.192 ±0.0024	0.0228
4	36	20	1341	44.7	13±1.9	1.7
13	34	22	1182	39.4	15.1±2.8	1.8
14	31	25	1075	35.8	84.2±6.8	9
15	28	28	753	25.1	940±370	70.8
16	25	31	275	9.2	to large to measure	-

From the resistivity value in Table 3.1, an assumption can be made: with increasing N_2 flow, the film changes from aluminum[1] to aluminum rich Al-N film (it can

[1] Resistivity of pure aluminum is 2.82E-8 Ωm

be named as self-doped aluminum nitride). Further increase in N_2 flow makes more aluminum react with nitrogen. The film resistivity increases almost exponentially (See Figure 3.1) when nitrogen gas flow is larger than 14sccm. This means the structure of Al-N layer has been changed. The growth rate is relatively low in partially crystallized Al-N (sample 16) because crystallization is an energy consuming process.

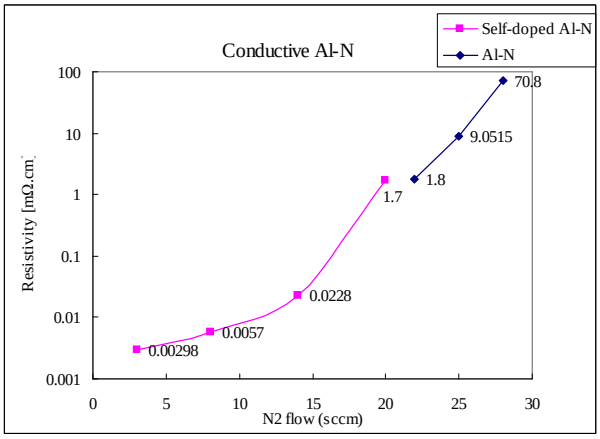

Figure 3.1: Electrical resistivity of the films against nitrogen flow

3.1.2 Sputtering Parameters Influence on Al-N Films Internal Stress and Resistivity

Using recipe for sample 15 as a basic recipe, the influence of sputtering power, bias, temperature on the film residual stress is investigated. Because film growth rates are known from Table 3.1, 300nm thick film can be sputtered by adjusting the sputtering time.

Table 3.2: Effects of (a) substrate temperature, (b) DC power, (c) substrate bias on film resistivity and residual stress

(a) Effects of substrate temperature. (Ar/N_2= 28/28, film thickness=300nm, DC power=2kW, substrate bias=0W, t= 2min)

Sample No.	Temperature (°C)	Stress (MPa)	Resistivity ($m\Omega \cdot cm$)
22	150	68	24.18
15a	300	30	70.4
27	450	-52	900

(b) Effects of DC power. (Ar/N_2= 28/28, film thickness=300nm, temperature=300°C, substrate bias=0W)

Sample No.	DC power (kW)	Deposition time	Stress (MPa)	Resistivity ($m\Omega \cdot cm$)
23	1	1min	231	-
15a	2	2min	30	70.4
24	4	4min	91	2.36

(c) Effects of substrate bias. (Ar/N_2= 28/28, film thickness=300nm, temperature=300°C, DC power= 2kW, t=2min)

Sample No.	Bias (W)	Stress (MPa)	Resistivity ($m\Omega \cdot cm$)
15a	0	30	70.4
28	0~25	-114	2280
25	50	-339	18900
26	100	-512	111900

Table 3.2 (a) to (c) shows resistivity and stress variation with temperature, power and bias, respectively. As temperature (and/or bias) rises, the residual stress become more compressive and the resistivity is larger. Increasing sputtering power also has a positive effect on decreasing ρ, but the stress curve drops dramatically and rebounds a little bit when power was boosted from 2kW to 4kW(Figure 3.2)

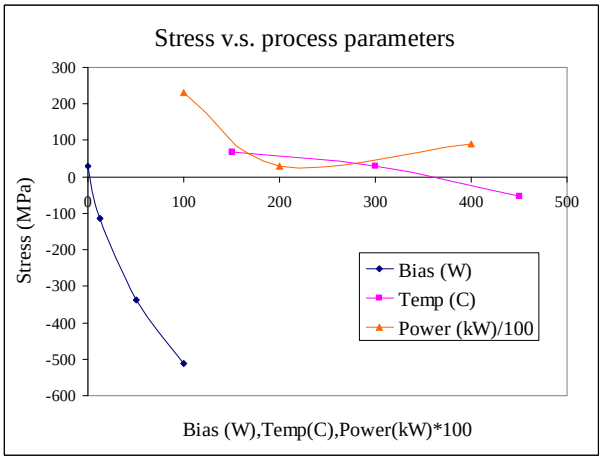

(a)

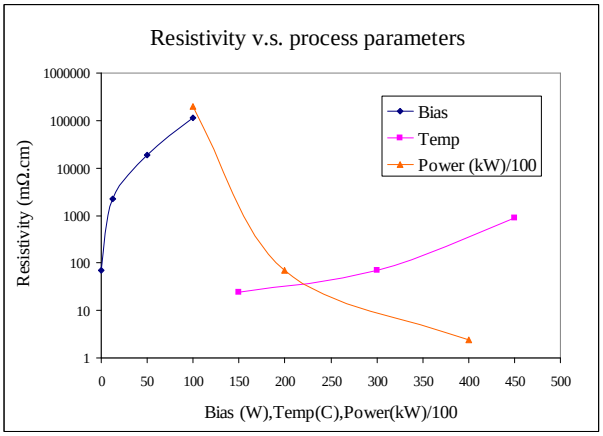

(b)

Figure 3.2: (a) Internal stress and (b) resistivity of Al–N films as functions of sputtering parameters

Taking both resistivity and stress into consideration, zero bias leads to less compressive stress but not very high resistivity. A 300°C sputtering temperature also guarantees the film stability in the following fabrication steps.

3.1.3 Reproducibility of Sputtering Al-N Sample

In order to examine the reproducibility of the sputtering process, a couple of samples were sputtered repeatedly with the same recipe.

Table 3.3: DC magnetron sputtering Al-N film's reproducibility results

Sample No.	Ar (sccm)	N_2 (sccm)	DC Power (kW)	Thickness (nm)	Resistivity ($m\Omega \cdot cm$)	Stress (MPa)
15	28	28	2	753	70.8	-
15'	28	28	2	843	71.52	0.7
24	28	28	4	440	2.36	91
24'	28	28	4	437	2.69	73.3
52	31	25	2	308	34.92	0.7
52'	31	25	2	308	38.56	4.3
53	31	25	4	358	2.04	0.7
53'	31	25	4	358	2.62	69.1

From Table 3.3, good reproducibility of film resistivity and stress can be achieved. Furthermore, the residual stress indicates that very low stress films (0.7MPa tensile stress) can be obtained.

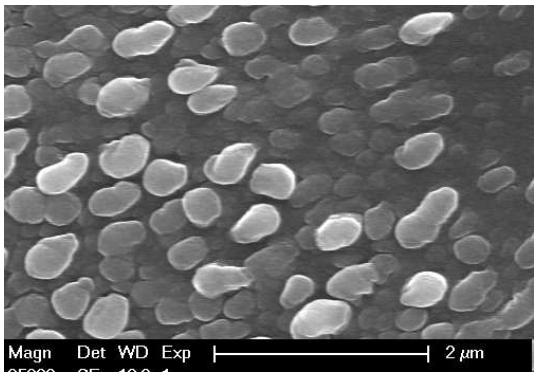

(a) Al-N sample 15

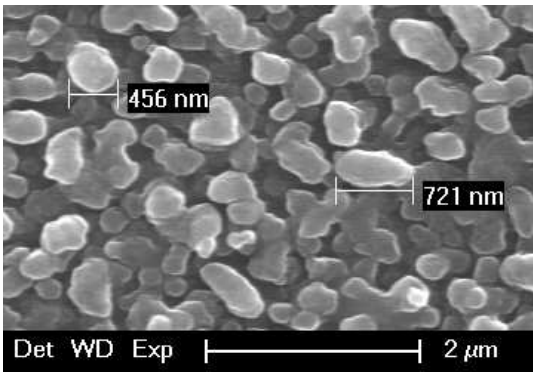

(b) Al-N sample 24

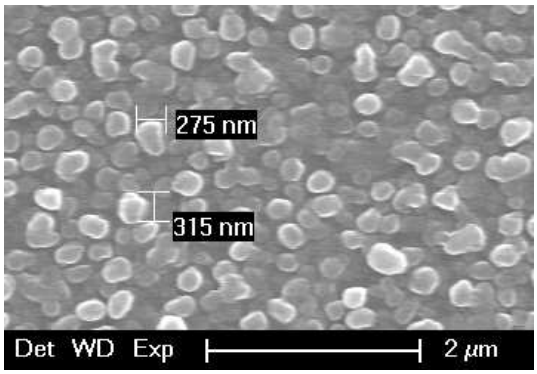

(c) Al-N sample 52

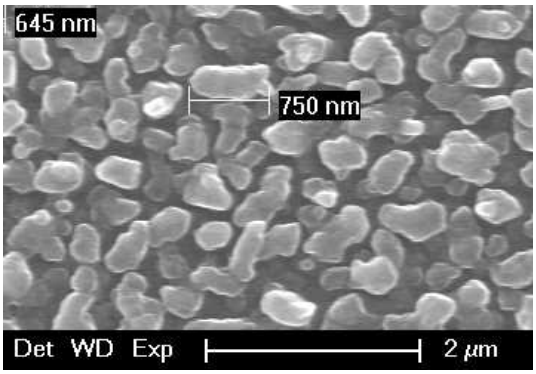

(d) Al-N sample 53

Figure 3.3: Surface morphology of conductive Al-N (same magnification)

From Figure 3.3, we can see that conductive Al-N have a rough surface and size of pebble-like structure affects the resistivity of the sample. Samples with larger

pebble structure have lower resistivity (sample 24 and 53), while smaller pebbles cause larger resistivity (sample 52).

3.2 TCR Measurement

As mentioned in Chapter 2, VanderPauw structures are needed to get accurate resistance value at a certain temperature. These structures need to be fabricated by properly patterning the AlN thin film.

3.2.1 Al-N Patterning and Metalization

The schematic drawing of the aluminum nitride process flow is depicted in Figure 3.4

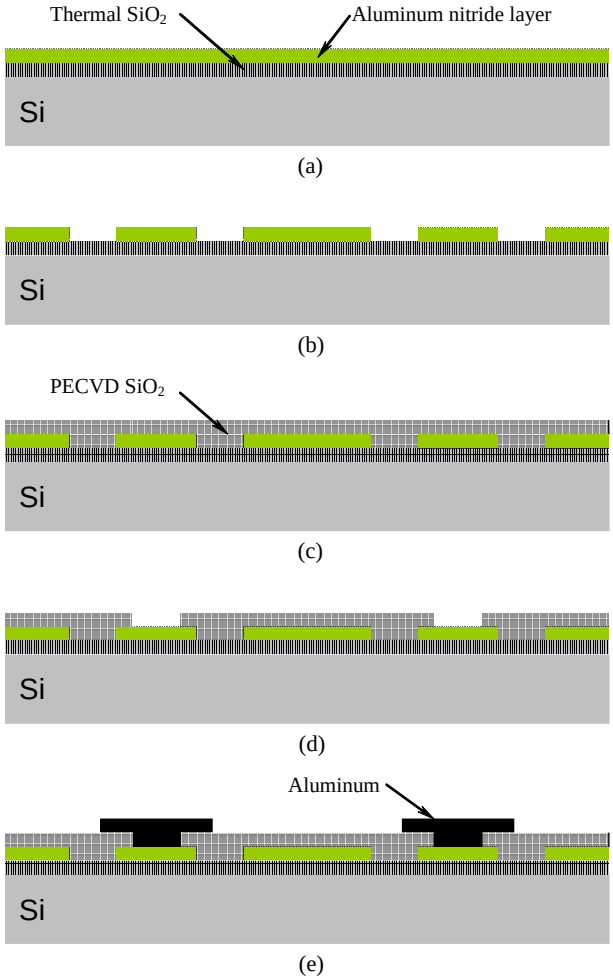

Figure 3.4: Fabrication flow of Al-N (not to scale)

Aluminum nitride film on top of thermal silicon oxide layer was first etched by MF322 developer at 70°C with standard mask PDM18_LP (Figure 3.4 (b)). Afterwards, 800nm silicon oxide was deposited at 400°C by PECVD. Next, contact openings were defined in mask PDM18_DO and they were etched as in Figure 3.4 (d) by fluorine plasma. At last, 1475nm aluminum layer was sputtered and patterned (Figure 3.4 (e)) to provide the electrical connection for the measurement.

3.2.2 TCR Results

By using VanderPauw structures, resistance of the film at various temperatures can be measured. If the data can be fitted with a linear equation, the slope of the curve divided by sheet resistance at 25 $°C$ is α_{tcr}. An example of TCR measurements result is plotted in Figure 3.5.

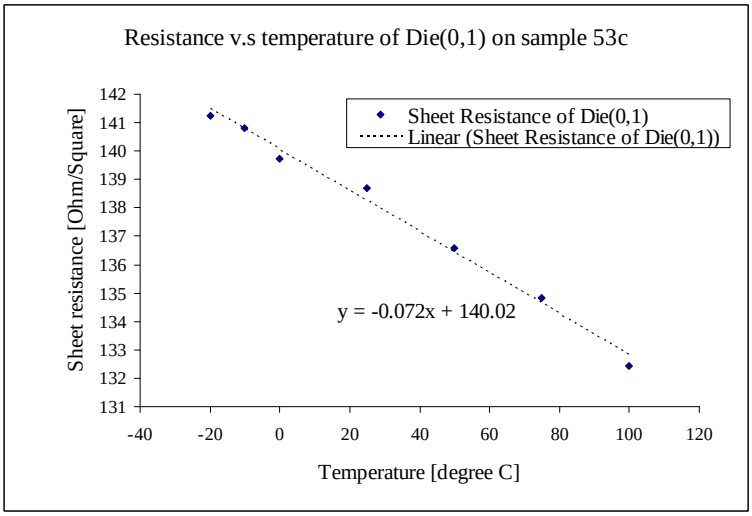

Figure 3.5: Resistance versus temperature plot of Die (0,1) on sample 53c, α_{tcr}=-0.072/138.69954=-519.12ppm/$°C$

The film resistance on the wafer is not uniform, so eight monitoring points[2] were chosen to examine TCR values on each sample. Results on Al-N sample 53 are listed as an example in Table 3.4.

Sample No.	Die	$R_{\square}(\Omega/\square)$	α_{tcr}(ppm)
53c	(0,-4)	83.42	-389.6
	(0,-3)	119.51	-612.5
	(0,-2)	89.78	-507.9
	(0,-1)	115.33	-591.32
	(0,0)	159.81	-413.0
	(0,1)	138.70	-519.1
	(0,2)	93.97	-439.5
	(0,3)	88.43	-410.5

Table 3.4: TCR results on different dies, Al-N 53c

Al-N samples have negative TCRs, which means these films have semiconductor properties. This can be explained by the fact that wurtzite aluminum nitride is a compound semiconductor.

[2]TCR were measured on 8 dies per wafer. They are (0,-4), (0,-3), (0,-2), (0,-1), (0,0), (0,1), (0,2), (0,3). The coordinates corresponding die locations can be found in Appendix B.

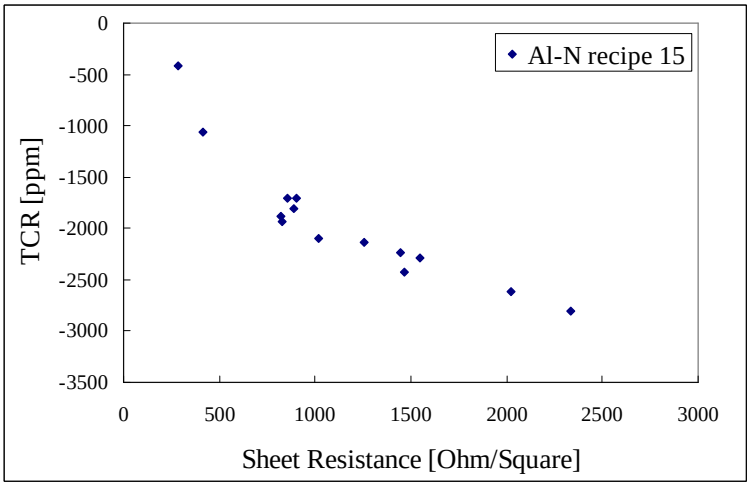

(a)

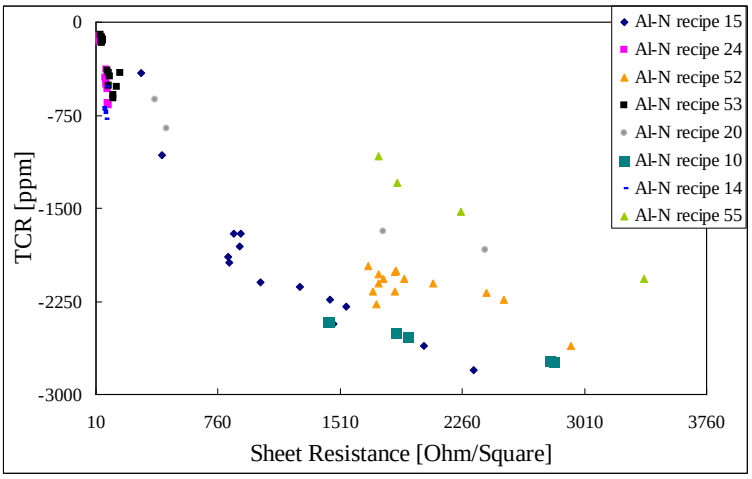

(b)

Figure 3.6: Influence of sheet resistance on TCR, (a) recipes 15 as an example, (b) all recipes integrated together

However, from the Figure 3.6, the TCR was found to be more negative for films with larger resistance. This increasingly more negative TCR at higher ohms per square is the normal behavior in metal films [40]. So $R_{\square}$ influence on TCR means these films also possess metallic properties, which could be interpreted as follows. Not all aluminum atoms are bonded with nitrogen atoms to form crystals, and this results in Al-N metallic behavior.

From the TCR results[3], the conclusion of not highly crystallized Al-N films possessing both the properties of aluminum and wurtzite AlN can be drawn.

In this chapter, the low internal stress, conductive Al-N thin films fabrication were discussed, and TCR values of some of the samples were measured. The gauge factor test results of Al-N samples are reported together with Cr-N devices in Chapter5.

[3]Referring detailed results in Appendix A

4 Thin Film Chromium Nitride

4.1 Sample Preparation

Chromium nitride is a good coating material for metal and plastic due to its high hardness, good oxidation resistance, and low coefficient of friction. RF and DC reactive sputtering is frequently used by many researchers [41, 42, 43, 44] to deposit thin films of CrN. Because both the target and the product are conductive, the simple and fast sputtering - DC magnetron reactive sputtering in argon and nitrogen gas ambient was adopted in this study to prepare the chromium nitride layers.

4.1.1 Film Deposition

The sputtering machine used for Cr-N deposition was also Aviza Sigma 204 in Dimes laboratory. The starting material is (100) p-type silicon wafers with 100nm thermal oxide on top. The substrate was fixed 75mm below the 99.95% chromium target. Before the sputtering starts, the chamber was pumped down to 7×10^{-5} mTorr.

The first test run was to investigate the effect of gas ratio on the resistivity of the film. Five samples were sputtered in different gas mixture. Target DC power, substrate temperature, total gas flow and deposition time were set at 2kW, 200°C, 112sccm and 5min, respectively. During the deposition, the flow rate of each gas was controlled independently but the total gas flow maintained at 112sccm, which sustained 4.5mTorr pressure in the chamber. Deposition rates were calculated according to the thickness measurement, and the resistivity distribution on wafer scale was measured by four-point probe method.

Table 4.1: Sputtering recipe design to test CrN electrical resistivity

Sample No.	Ar (sccm)	N_2 (sccm)	Thickness (nm)	Deposition rate ($\mathring{A}/(kW \cdot min)$)	$R_\square$ ($\Omega/\square$)	Resistivity ($m\Omega \cdot cm$)
1	112	0	1115	1115	0.166±0.002	0.0185
2	90	22	797	797	1.210±0.0025	0.096
3	67	45	735	735	2.2±0.1059	0.16
4	50	62	562	562	16.9±0.6	1
5	38	74	516	516	556±22	28.7

From Figure 4.1, we can see clearly that the thin film resistivity increases with the nitrogen partial pressure. Sample 1 is gray shiny like pure chromium and the resistivity ($18.5\mu\Omega \cdot cm$) is slightly higher than bulk chromium value which is $13.2\mu\Omega \cdot cm$. The sputtering conditions are comparable with those reported by Tsuchiya [45], Gall [46] and Martinez [47]. Their substochiometric chromium nitride ($CrN_{0.93\sim0.98}$) was in the range of $1.2\tilde{}7m\Omega \cdot cm$, while overstochiometric $CrN_{1.05\sim1.15}$ layers have resistivity at room temperature of $12\tilde{}40m\Omega \cdot cm$. At the same time, Bhushan reported the resistivity of stoichiometry bulk CrN to be $0.64m\Omega \cdot cm$ [48]. All these tell us that sample 5 was a nitrogen-rich chromium nitride film.

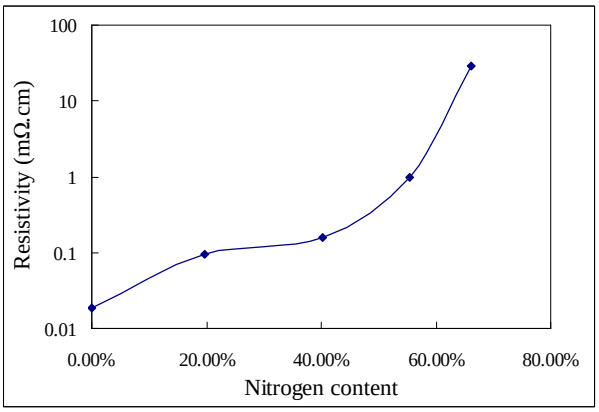

Figure 4.1: Variations of CrN thin film electrical resistivity v.s. nitrogen content

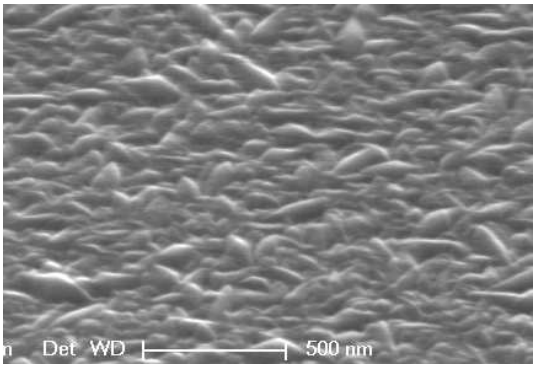

(a) Surface morphology of Cr-N sample 3

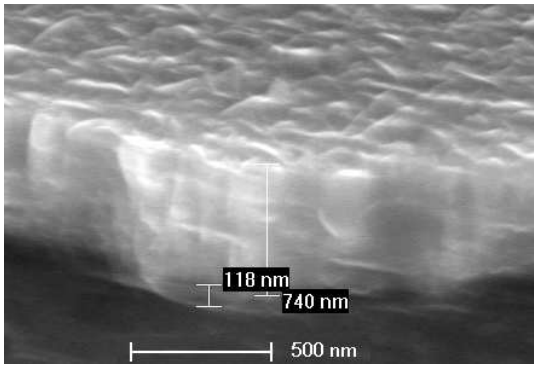

(b) Cross section of Cr-N sample 3

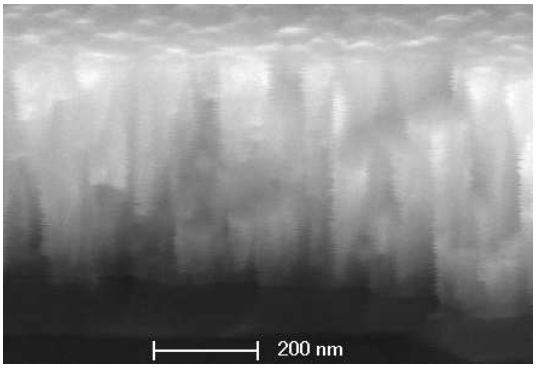

(c) Cross section of Cr-N sample 4

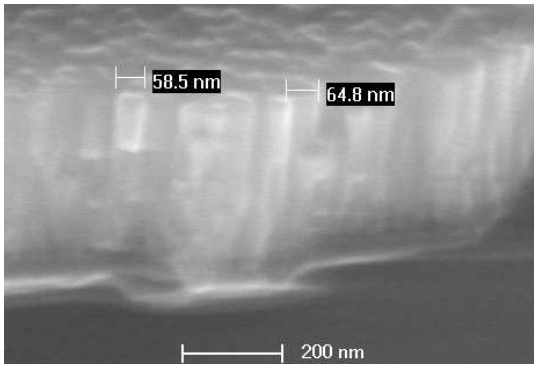

(d) Cross section of Cr-N sample 5

Figure 4.2: SEM micrograph of Cr-N thin-films of different recipes

From the SEM pictures in Figure 4.2 we can tell that sample 3 is poly crystalline CrN without an obvious crystal orientation, while from the cross section of sample 4 and 5 we can see the grain boundaries clearly. (As x-ray diffraction measurement hasn't been carried out yet, only a qualitative analysis of the layer is reported here.) However, Inoue found out that with nitrogen pressure increase, single phase (111) CrN with a dominating an NaCl-type was obtained [49]. In addition, Chekour's study explains the growth mechanism, and when the thickness of the film is larger than 300nm, , independently of the bias during sputtering, good (111) polycrystalline chromium nitride is grown [42]. Considering these studies and the SEM cross section

[41, 42], we can conclude that we can use the recipe of sample 5 as a basic recipe to grow almost (111) single phase, slightly overstochiometric, high resistivity chromium nitride films.

4.1.2 Sputtering Parameters Influence on Cr-N Films Internal Stress and Resistivity

Resistivity and residual stress are affected not only by gas ratio, but also by other sputtering parameters. Using a similar procedure, sputtering recipes were designed to deposit 300nm CrN films (See Table 4.2) and study the effect of substrate temperature, DC power and substrate bias.

Table 4.2: Effects of (a) substrate temperature, (b) DC power, (c) substrate bias on film resistivity and residual stress

(a) Effects of substrate temperature. (Ar/N_2= 38/74, film thickness=300nm, DC power=2kW, substrate bias=0W, t= 2min 54sec)

Sample No.	Temperature (°C)	Stress (MPa)	$R_\square$ ($\Omega/\square$)	Resistivity ($m\Omega \cdot cm$)
5	100	449	819±19	24.57
6	200	524	749±36	22.47
7	350	706	720±22	21.6
8	500	963	455±32	13.65

(b) Effects of DC power. (Ar/N_2= 38/74, film thickness=300nm, temperature=25°C, substrate bias=0W)

Sample No.	DC power (kW)	Deposition time	Stress (MPa)	$R_\square$ ($\Omega/\square$)	Resistivity ($m\Omega \cdot cm$)
12	4	1min27sec	-672	4.8±0.1	0.14
10	2	2min54sec	333	714±22	21.4
11	1	5min49sec	220	633±11	19
13	0.5	11min38sec	146	676±16	20.3

(c) Effects of substrate bias. (Ar/N_2= 38/74, film thickness=300nm, temperature=25°C, DC power= 0.5kW, t=11min 38sec)

Sample No.	Bias (W)	Stress (MPa)	$R_\square$ ($\Omega/\square$)	Resistivity ($m\Omega \cdot cm$)
14	20	110	645±20	19.4
15	40	103	574±15	17.2
16	80	110	382±3	11.5

Resistivity and residual stress versus sputtering parameters are plotted in Figure 4.3. Substrate temperature and DC power have positive effect on tensile stress of overstochiometric chromium nitride films, while increasing bias power from 20W to 80W doesn't seem to make much difference. On the contrary, the bias is the only factor which has substantial influence on the resistivity. Eventually, with gas ratio (Ar/N_2) of 38/74, 0 or 20W bias and 500W DC power supply, several Cr-N thin film layers are sputtered on a substrate at a temperature of 200°C (See Table 4.3).

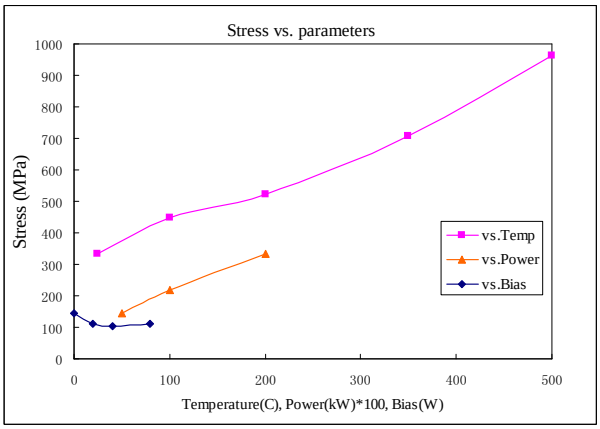

(a)

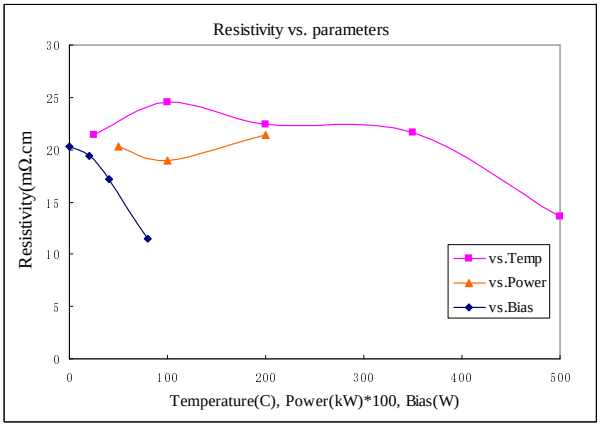

(b)

Figure 4.3: (a) Internal stress and (b) resistivity of Cr–N films as functions of sputtering parameters

Table 4.3: Recipes of interest (500W DC power supply, 200°C substrate)and properties of the sample

Sample No.	Ar (sccm)	N_2 (sccm)	Deposition time	Bias (W)
17	44	68	11min20sec	0
18	38	74	11min38sec	0
19	38	74	11min38sec	20

	Stress (MPa)	Film thickness (nm)	$R_\square$ ($\Omega/\square$)	Resistivity ($m\Omega \cdot cm$)
17	+294	275	933.27±10.23	25.66
18	+276	282	763.48±12.20	21.53
19	+245	260	692.75±15.05	18.01

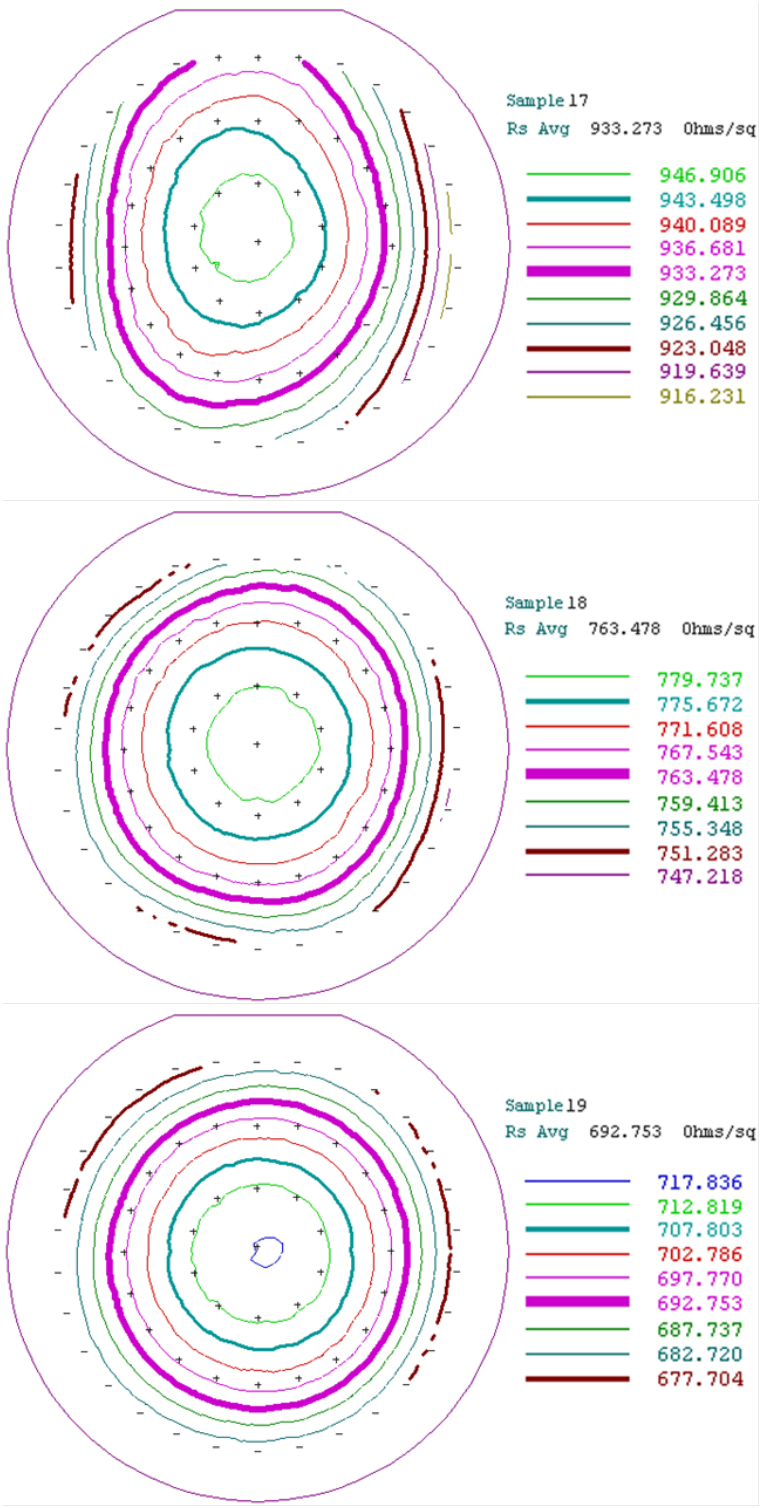

Figure 4.4: Contour maps of Cr-N sample 17, 18 and 19

The uniformity information was obtained from the contour map. For sample 17, 18 and 19, the contour maps are given in Figure 4.4. Relatively uniform resistance distribution was achieved. So it can be concluded that uniform chromium nitride can be obtained by DC magnetron sputtering and sheet resistances in the central area are slightly larger than that at the edge of the wafer.

Sample 17, 18 and 19 are relatively high resistivity and low tensile stress samples. In addition in Figure 4.5, grain boundaries are clearly pictured and they present good columnar structure. What's more, the boundary between 100nm silicon dioxide and Cr-N are obvious. These three samples have very similar surface morphology, so only the surface image of one sample is included here.

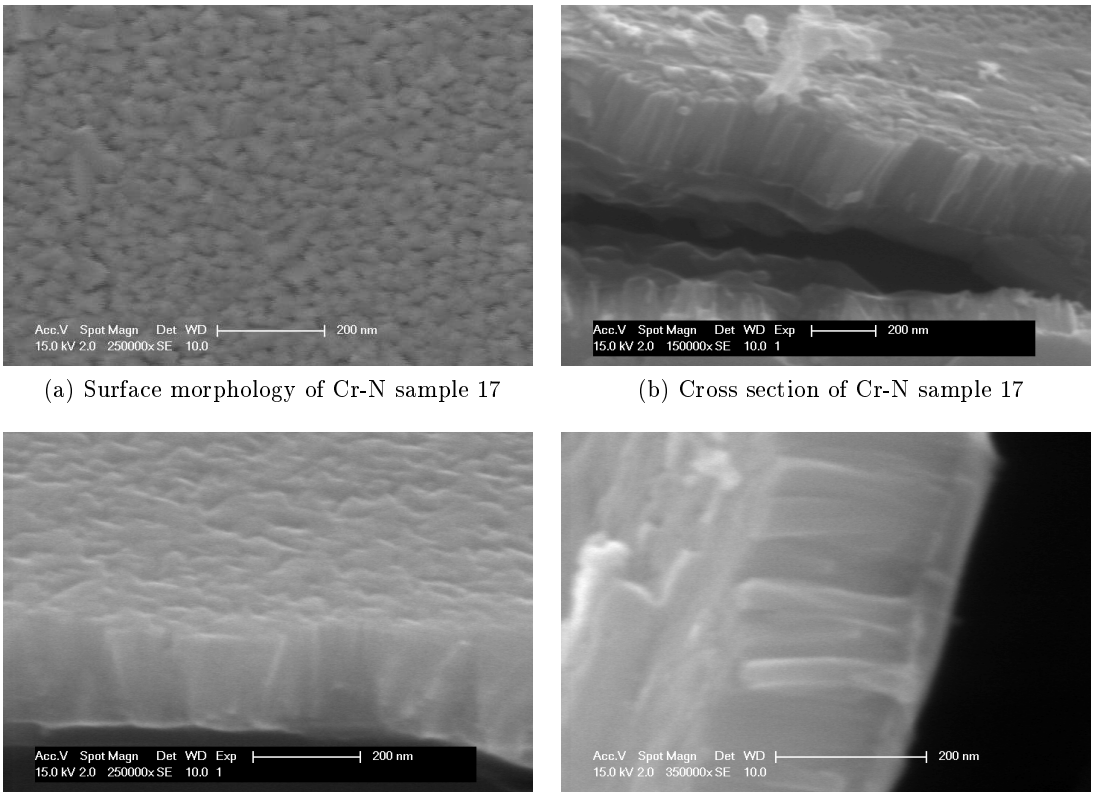

(a) Surface morphology of Cr-N sample 17

(b) Cross section of Cr-N sample 17

(c) Cross section of Cr-N sample 18

(d) Cross section of Cr-N sample 19

Figure 4.5: Scanning electron microscopy of scratched area of chromium nitride sample (a)(b)17 (c)18 and (d) 19

4.1.3 Long-term Stability

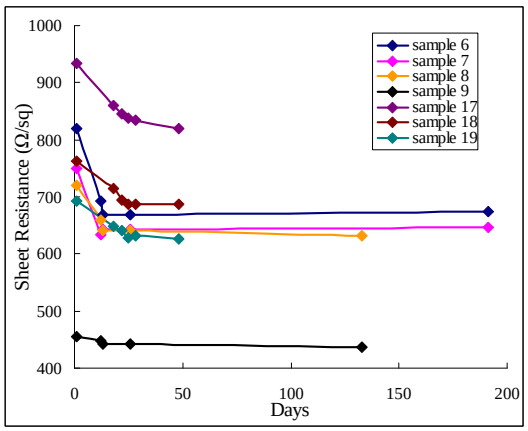

Figure 4.6: Sheet resistance as function of time

An unfavorable phenomenon was observed during sample preparation. The sheet resistance value of different samples measured in a large span of time showed that the value is not a constant vs. time. A rapid resistance drop was observed at first. About one month later, the sheet resistances of the films become stable. It can be seen more clearly in the plot in Figure 4.6.

From the SEM pictures of Cr-N samples (Figure 4.5) we can see clearly that they didn't have a very dense structure but porous columned structure. This gave the chance of gas molecules to interchange and maybe some dangling bond attracted some molecules and/or reacted. However the quantity was not substantial enough to change the surface morphology or the volume of the sample. The most probable participants are oxygen and water molecules, and when most bond are saturated, the electrical resistivity drop fades out.

Certainly, we can accelerate this process without changing the property of the sample by a high temperature annealing in nitrogen ambient. But high temperature (at least higher than 600°C, usually higher than 900°C to provide enough energy is unwelcome. Low temperature (200°C) thermal annealing was also tried for 48h, but it didn't make any difference.

Another slight possibility is the argon atoms which were trapped during the sputter deposition process escaped slowly and had some effect on the crystal structure.

4.2 VanderPauw Structures Fabrication Flow

In Chapter 2, the method of implementing TCR measurement was introduced. In order to get accurate measurement results, fabrication of VanderPauw structure is necessary. Although the same fabrication process flow as for Al-N (see section 3.2.1) was used here, a few issues related to potential Cr contamination of equipment and some unexpected problems with etching selectivity were encountered. These are discussed here before the TCR measurements are reported.

4.2.1 Safety Issues during Fabrication

Chromium is not a standards material in DIMES laboratory, so is chromium nitride. Before fabrication, the flow chart of Cr-N should be assembled in such a way to avoid contamination to the equipment.

4.2.2 Etchant Selection

Hydrogen peroxide and chromium etchant Cr10 (HNO_3/NH_3CrNO_3) were chosen for the etching test. There was no effective etching in the H_2O_2 solution, while the etch rate of CrN in Cr10 solution is relatively high. In order to get a reasonable etch rate, 60ml Cr10 were diluted in 180ml DI water. After immersing the sample in this solution for 5 minutes, no chromium nitride was left on the wafer. The concentration of the effective etchant would decrease with etching, and in addition, the etch rate of CrN films prepared in various conditions were slightly different, so the etch time should be determined by checking the color change visually. Thus when the gray shinny metal color disappeared and the layer became purple (100nm silicon oxide), the etch time is enough.

Table 4.4: Sheet resistance measured at different times

Sample No.	10-12-2009	21-12-2009	22-12-2009	04-01-2010	21-04-2010	18-06-2010
6	819±19	693±10	668±9	668±9		674.93±9.22
7	749±36	633±29	643±28	643±28		647.35±27.84
8	720±22	659±23	642±23	642±23	632.01±35	
9	455±32	447±38	442±37	442±37	437.28±31	
Sample No.	26-03-2010	12-04-2010	16-04-2010	19-04-2010	22-04-2010	12-05-2010
17	933.27±10.23	860.01±7.09	846.02±34.39	838.76±31.89	834.61±40.48	818.74±46.81
18	763.48±12.20	714.77±9.74	69.26±44.29	687.03±45.26	687.13±48.85	686.84±47.87
19	692.75±15.05	649.31±12.15	641.55±29.14	629.11±34.53	632.29±34.38	626.12±33.72

Dry etching is also possible for etching chromium nitride sample. In reference[50], Iba used Cr-N layer as a hard mask, and his way of "developing" this mask layer is using Cl_2 and O_2 plasma in an ICP system. In our laboratory, Trikon Ωmega 201 plasma etcher was used as a metal dry etcher (usually for aluminum and titanium dry etching). But because of the physical bombardment during dry etching, chromium particles contamination will be left behind. So dry etching is not currently possible in Dimes.

4.2.3 Problems during Processing and Solutions

4.2.3.1 Resistance of Cr-N to dry etching in F-base chemistry

In the standard fabrication flow (See Figure 3.4), after PECVD silicon oxide deposition, metal contact area were opened by dry etching during which 30% over etch is necessary. Thus, whether fluorine based etchant gases etch the Cr-N layer or not is an important issue. A wafer with chromium nitride was then used for this test. The sheet resistance before and after 5 minutes dry etching in Alcatel F-etcher GIR 300(recipe: PECVD SiO_2[1]) was measured.

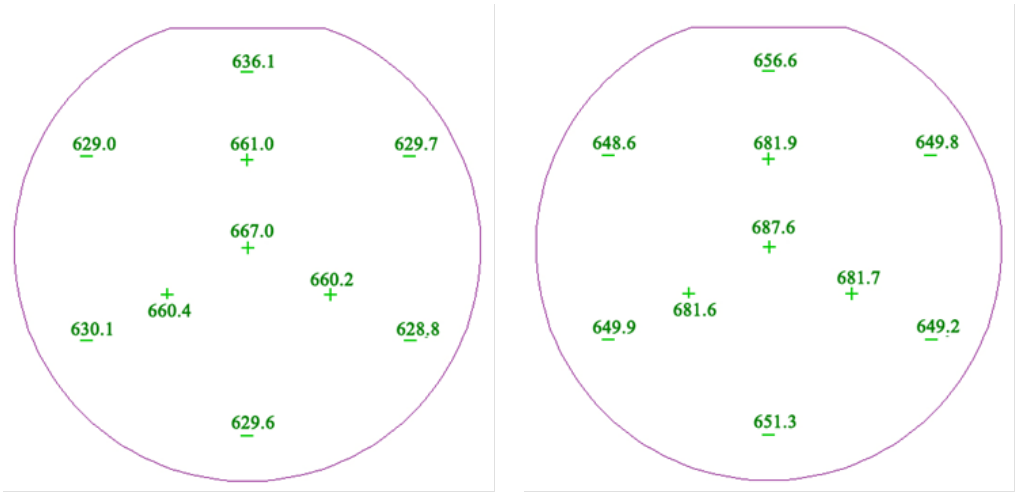

(a) Before etching: $R_{\square}$=643.2Ω/□ (b) After etching: $R_{\square}$=663.81Ω/□

Figure 4.7: Sheet resistance of Cr-N before and after etching

The sheet resistance value only changed from 643.2Ω/□ to 663.81Ω/□. It means that if the thickness of the sample is 300nm, less than 10nm CrN were removed during 5 min etching, which is negligible. This test confirmed that during the PECVD silicon oxide etching, Cr-N will not be significantly etched or affected.

4.2.3.2 Resistance of Al in Cr-N wet etchant

The resistance of Al in diluted (25%) Cr10 solution was measured by immersing a test wafer coated with aluminum for 5 min in this solution.

[1] $CF_4/CHF_3/He$=50/25/40sccm, Pressure=0.05mbar, RF power=60W, PECVD SiO_2 etch rate=39nm/min

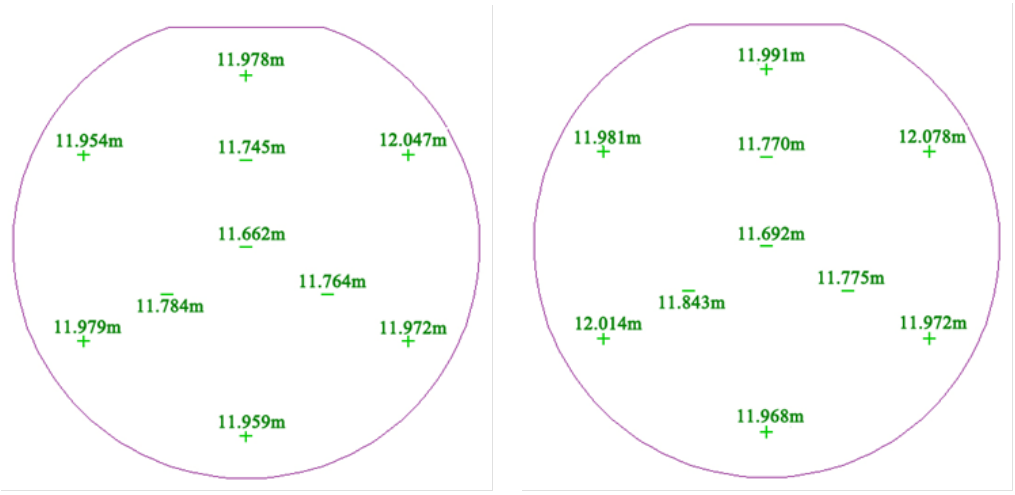

(a) Before etching: $R_{\square}$=11.88$m\Omega/\square$ (b) After etching: $R_{\square}$=11.9$m\Omega/\square$

Figure 4.8: Sheet resistance of aluminum layer before and after etching

From the sheet resistance measurement reported in Figure 4.8, we can say that the aluminum layer will not be etched in diluted Cr10 etchant in the above mentioned conditions.[2].

4.2.3.3 Resistance change after PECVD SiO_2 deposition

The fabrication was started on the deposited Cr-N samples 17, 18 and 19. However, a problem emerged when we measured the resistance on VanderPauw structure. After completing the process, the sheet resistance increased significantly and uniformly on the whole wafer (See Table 4.5 and die measurement result in 6). After ruling out the possibility of measurement equipment error, changes must have happened on these samples during the processing.

Sample No.	$R_{\square}$ ($\Omega/\square$) by CDE ResMap before processing (12-05-2010)	$R_{\square}$ ($\Omega/\square$) of VanderPauw structure (31-05-2010)
17	818.74±46.81	~2200
18	686.84±47.87	~1700
19	626.12±33.72	~1390

Table 4.5: Sheet resistance increment of Cr-N sample 17, 18 and 19

There could be two main reasons for the sheet resistance change:

1. The thickness of the Cr-N layer is reduced.

   Because the value of $R_{\square}$ increased more than a factor of 2, the thickness of the sample should reduce to 150nm or less. However, step measurement on Cr-N 17, 18, 19 before and after Cr-N etching showed no difference. (See also Figure 4.9, this is a repeated test.)

[2]This test is the preparation for reverse flow chart of Cr-N processing latter.

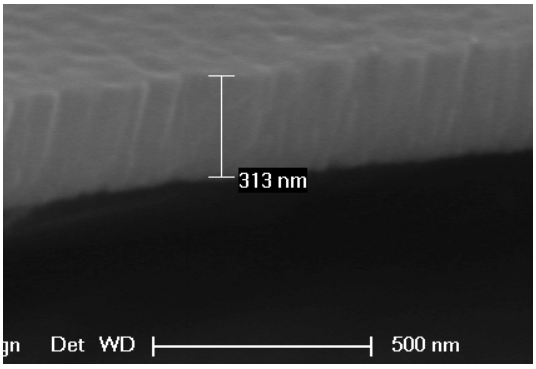

(a) SEM of scratched area of sample 8 before SiO_2 deposition. thickness is about 310 nm.

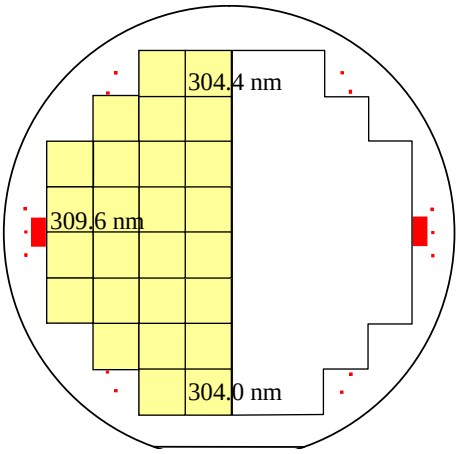

(b) Sample 8 after SiO_2 deposition, removal and half of the wafer was patterned. Step measurement results on patterned Cr-N are shown in the graph. Thickness is still about 305nm

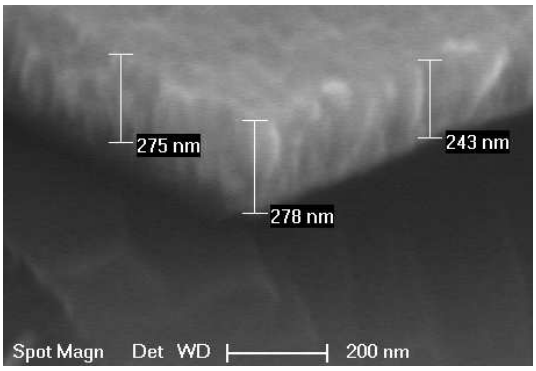

(c) SEM of scratched area of sample 21 before SiO_2 deposition. Thickness is about 270nm.

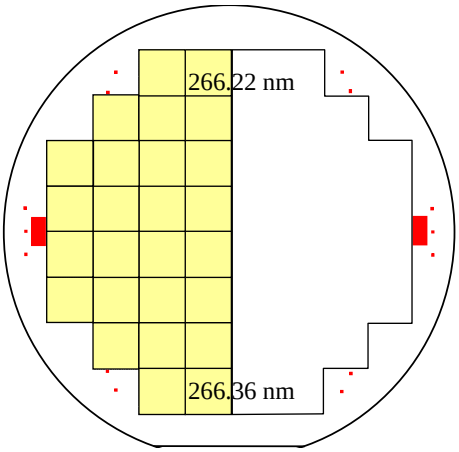

(d) Sample 21 after SiO_2 deposition, removal and half of the wafer was patterned. Step measurement results on patterned Cr-N are shown in the graph. Thickness is still about 270nm

Figure 4.9: Thickness after oxide layer removal of Cr-N sample 8 and 21

2. The electrical resistivity changes due to a change in sample properties during silicon oxide deposition.

   a) Higher temperature (400°C) during PECVD caused re-crystallization of Cr-N sample.

      To verify this assumption, Cr-N sample 8 (350°C sputtered)was chosen[3] to experience the silane oxide deposition and removal. If the assumption was correct,the resistance value should remain unchanged.

      The sheet resistance of sample 8 was originally 622.01±35.06 Ω/□, while after silane oxide deposition and removal, it became 1092.8±65.82Ω/□.

[3]The difference between PECVD temperature (400°C) and Cr-N 8 sputtering temperature (350°C) is only 50°C which is not large enough for Cr-N recrystallizing.

There was no possibility for crystal structure in sample 8 to change at silicon oxide deposition temperature, while the resistance value changed again. This is an indication that the assumption of resistance change due to recrystallization is not correct.

b) N_2O reacts with Cr or CrN forming Cr-O-N during the silicon oxide deposition

Because N_2O is one of the reactants[4] during silane oxide deposition and Mietus proposed a method of depositing Cr-O-N by using N_2O [51], this could be a reason of sheet resistance variance. So we deposited a Cr-N layer (sample 21) using exactly recipe Cr-N 19, and use a different source for the oxide deposition, i.e. TEOS(tetraethoxysilane)[5] instead of silane, to avoid the problem..

After the oxide removal, the resistance increased from 808.88±20.41 Ω/□ on June 7th to 1560.4±61.58 Ω/□ on June 9th indicating sheet resistance increase doesn't result from N_2O reacting with Cr or CrN.

It appears that none of the assumption for chromium nitride resistance change was valid.

As a result, the only possible reason could be deduced from the reference [16]. Yamadera reported that Cr-O-Si can be formed during PECVD and it is a conducting material [40]. Therefore the conclusion is:

During PECVD silicon oxide deposition process, oxygen and silicon atoms react with the chromium nitride layer and form a new compound material Cr-Si-O-N. To validate the conclusion, chemical composition analysis after PECVD oxide removal is needed.

4.2.3.4 Reverse fabrication flow

Because of the inevitable resistivity change during PECVD oxide deposition and patterning, the only solution is to reverse the process flow. Thus put the metalization layer underneath the chromium nitride layer. In fact, as indicated in 4.2.3.2, aluminum metal layer will be intact during Cr-N etching.

With a silicon wafer as a starting material, the main steps of the fabrication are:

1. Making alignment markers.
2. Dry oxidation of 100nm SiO_2.
3. 675nm Al/1%Si sputtering at $350°C$.
4. Resist coating, exposure with both M429_IC (job "g10a-1") and OPEN_10x10-V1 (job "g10a-edge (full)_ID2") reticles.
5. Development and Ωmega 201 plasma etching.
6. Resist strip by O_2 plasma and Al fence removal.
7. RF treatment to remove natural Al_2O_3 in HSE[6] module and then sputter Cr-N in Deposition module C in Aviza Sigma 204 system.
8. Resist coating, exposure with M429_GL (job "g10a-1") reticles.
9. Standard development and wet etching in 25% diluted Cr10.
10. Acetone spray resist removal and bath HNO3 99% cleaning.

The sketch of final version Cr-N process flow is in Figure 4.1.

[4] PECVD silane oxide: $3SiH_4+6N_2O \rightarrow 3SiO_2+4NH3_3+4N_2$
[5] $Si(OC_2H_5)_4 \rightarrow SiO_2+2H_2O+4C_2H_4$
[6] Hot Soft Etch

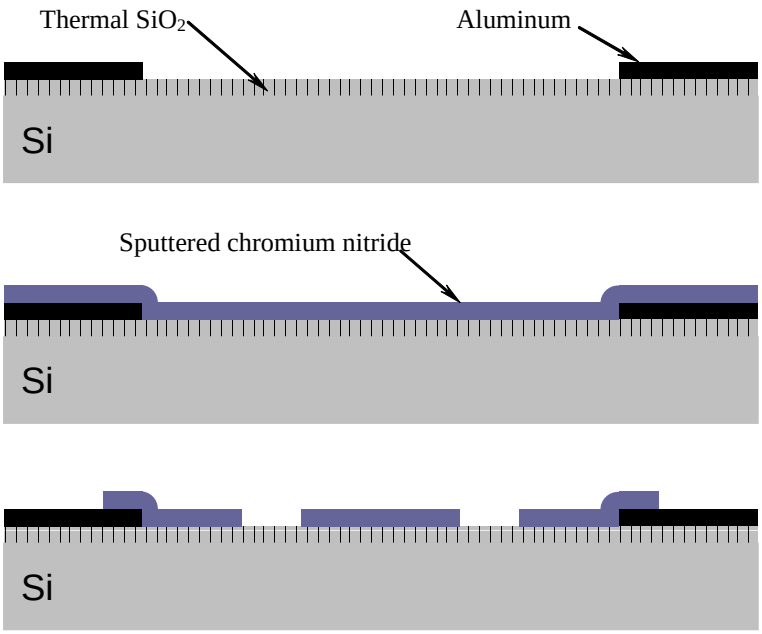

Figure 4.10: Fabrication flow of Cr-N (not to scale)

Film deposition recipes in step 7 were the same as Cr-N sample 18 and 19. These two samples were named Cr-N 18' and Cr-N 19'. From the resistivity in Table 4.6 we can see that the reproducibility of Cr-N thin films are very good.

Table 4.6: Cr-N thin film resistivity after sputtering

Sample No.	Film thickness (nm)	$R_{\square}$ ($\Omega/\square$)	Resistivity ($m\Omega \cdot cm$)
17	275	933.27	25.66
18	282	763.48	21.53
18'	286	755.51	21.61
19	260	692.75	18.01
19'	283	691.78	19.58

Coverage of sputtered chromium nitride was examined subsequently. Figure 4.11 shows that about 300nm Cr-N layers were deposited on 600nm[7] aluminum metal contacts. Good coverage were formed during the sputtering, and the growth direction of Cr-N grain seems to keep vertical to the substrate in SEM image.

[7] The thickness is enough for wire bonding and probe measurement

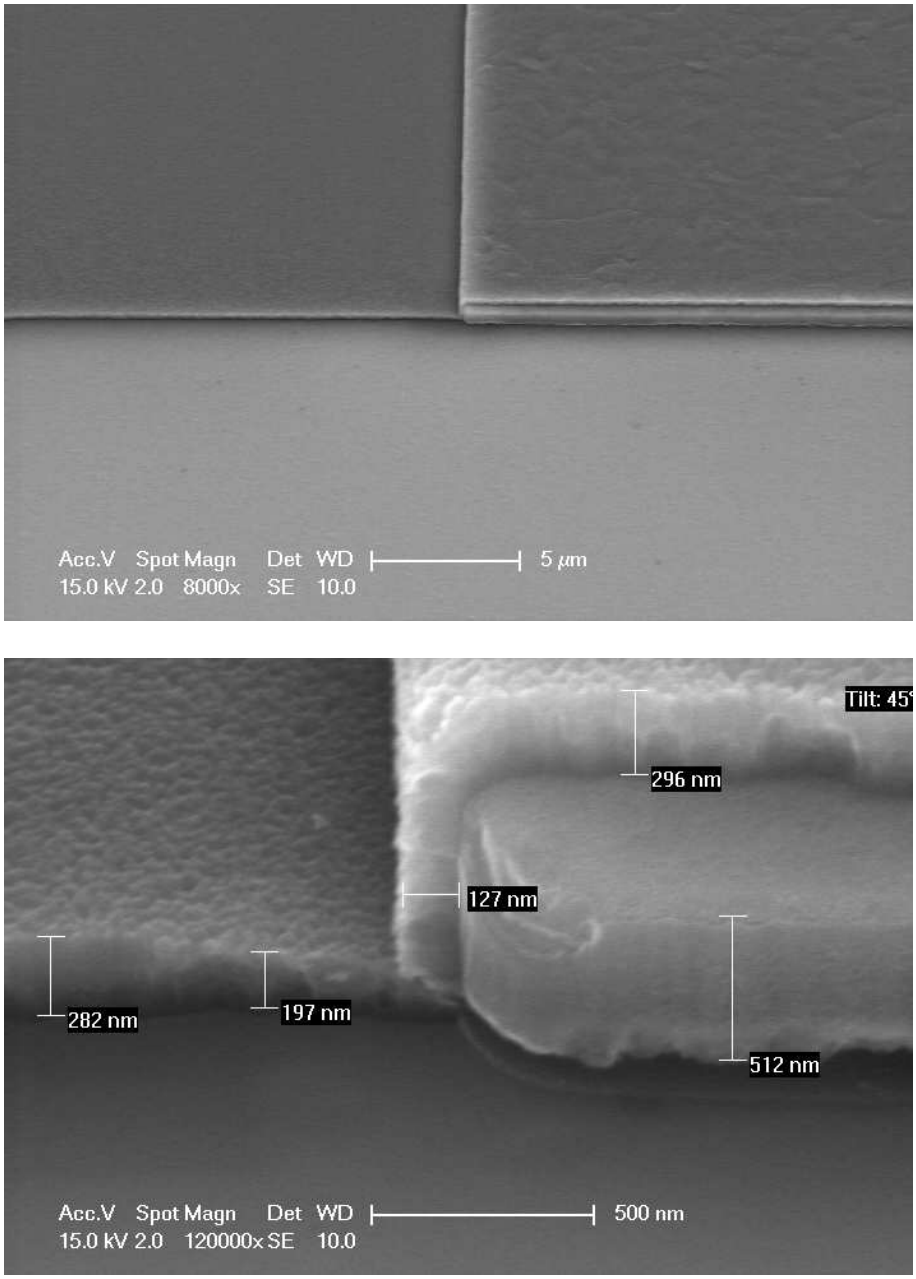

Figure 4.11: Cr-N coverage on 600 nm aluminum, the sample was deposited base on the recipe Cr-N19

4.3 TCR Measurement

4.3.1 Samples to be measured

Sample 17, 18 and 19 fabricated according to the standard flow and two more sample based on the recipe Cr-N 18 and Cr-N 19 fabricated as reverse flow were measured. The latter two samples were named sample 18' and 19', respectively. Due to the uniform resistance distribution, (see Figure 4.4), three dies (0,-4), (0,0) and (0,3)

were chosen to be measured on each sample[8].

4.3.2 Non-linear TCR Results

Resistance against temperature plot of Cr-N sample 17 is drawn in Figure 4.12. It is not a perfect linear function between $R_{\square}$ and temperature. The non linearity of Die (0,3) were calculated as in Table 4.6, It tells TCR calculated based on the slope of the linear fitting is not a good method to characterize the resistor's temperature sensitivity. However, from the temperature cycle process (See Figure 4.12 and Table 4.7), the hysteresis effect is too small to be significant.

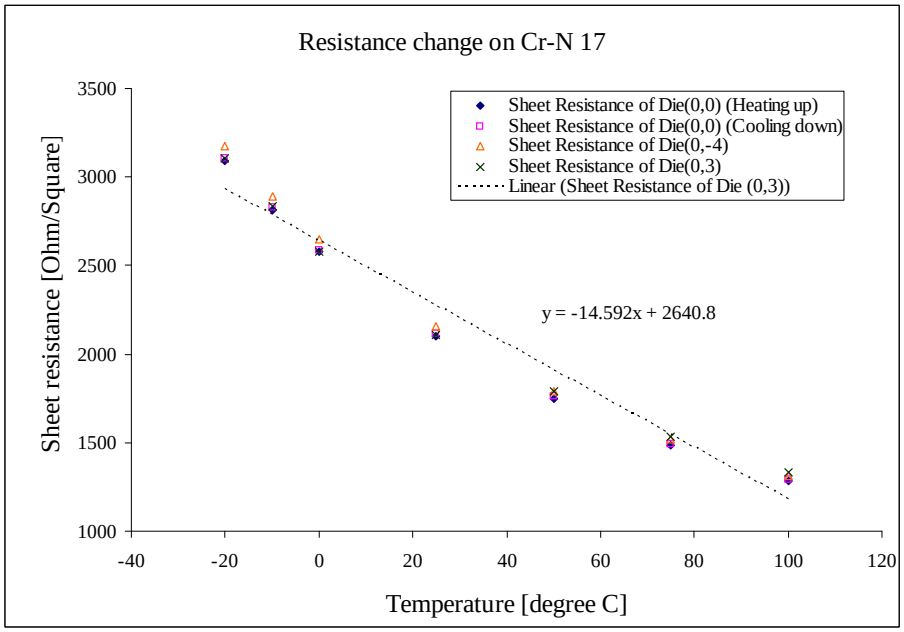

Figure 4.12: Resistance versus temperature plot of Cr-N sample 17

Table 4.7: Non-linearity of resistance change due to temperature on Die (0,3)

T ($^{\circ}C$)	-20	-10	0	25	50	75	100
$R_{\square}(\Omega/\square)$	3102.05	2834.6	2578.34	2104.68	1787.67	1533.77	1334.36
Linear curve fitting value y= -14.592x + 2640.8	2932.64	2786.72	2640.8	2276	1911.2	1546.4	1181.6
non-linearity	5.46%	1.69%	2.42%	8.14%	6.91%	0.82%	11.45%

Table 4.8: Hysteresis effect of temperature

CrN sample 17		-20$^{\circ}C$	-10$^{\circ}C$	0$^{\circ}C$	25$^{\circ}C$	50$^{\circ}C$	75$^{\circ}C$	100$^{\circ}C$
Die(0, 0)	$R_{\square}(\Omega/\square)$ Heating up process	3091.95	2812.09	2581.60	2102.42	1751.30	1487.70	1285.21
	$R_{\square}(\Omega/\square)$ Cooling down process	3107.76	2828.94	2589.21	2111.70	1758.77	1494.85	1294.22

[8]Die number rules see Appendix B

4.3.3 Curve fitting to B parameter equation

Because the linear approximation seems not to be appropriate to describe the resistance change in response to the thermal cycle, B parameter equation $R = R_0 \exp\left[B\left(\frac{1}{T} - \frac{1}{T_0}\right)\right]$ is used to fit the curve. Transform the equation into $\ln(R/R_0) = B\left(\frac{1}{T} - \frac{1}{T_0}\right)$, and the curves $\ln(R/R_0)$ v.s. $\left(\frac{1}{T} - \frac{1}{T_0}\right)$ were obtained. The slope of the curve is the B parameter. Larger B parameter means resistance decrease more quickly with increasing temperature.

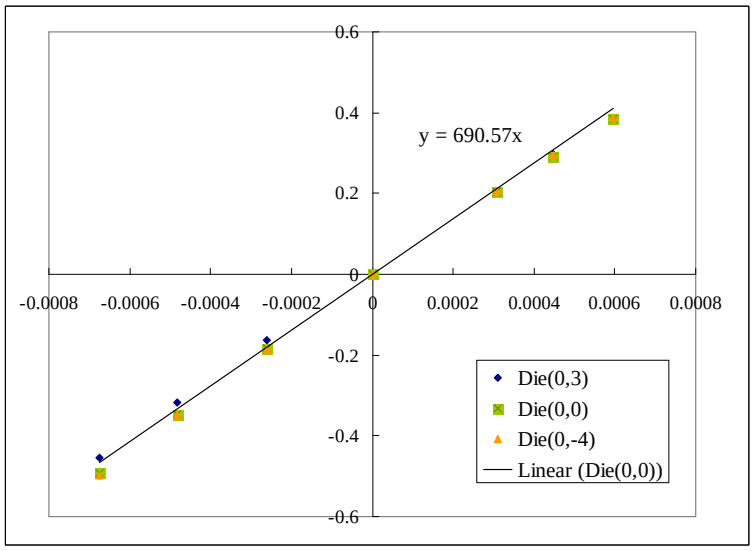

Figure 4.13: B parameter equation curve fitting for sample 17, B=690.57

From Figure 4.13, we can see B parameter equation can fit the data very well. The similar plot can be found in Constantin's work [52]. Temperature-dependent resistance measurements reveals the semiconducting behavior with hopping conduction, i.e. a negative temperature coefficient. In addition, Gall [46] and Constantin [52] had reported the band gap of Cr-N with (001) crystal orientation were 0.7eV and 0.071eV, which is another evidence of semiconducting property of Cr-N thin film.

B-parameter results for all 5 samples are listed in Table 4.9[9]. A plot of B parameter versus sheet resistance was drown in Figure 4.14. It shows linear relationships between B parameter and film resistance.

Table 4.9: B parameter of all Cr-N sample

	$R_\square(\Omega/\square)$	B
Sample 17	2102.42	690.57
Sample 18	1635.33	651.80
Sample 19	1353.29	635.49
Sample 18'	739.79	570.87
Sample 19'	680.41	568.61

[9]Curve fitting of other samples see Appendix A.

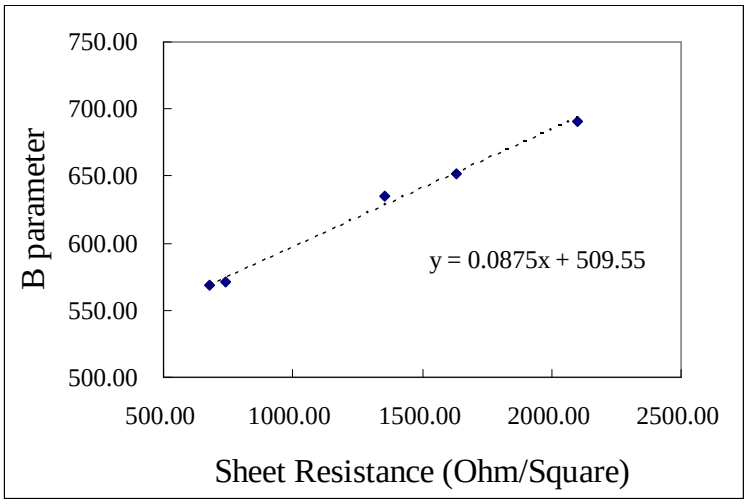

Figure 4.14: B parameter as a function against the resistance.

5 Mask Design and GF measurement

5.1 Mask Design

Wafer scale film resistance distribution, temperature coefficient, etc. have already been discussed and mentioned in the previous chapters. However, the most importance criterion of strain sensitive material selection is the gauge factor whose definition was specified in Chapter2. In order to acquire the sensitivity of resistance to micro strain, resistance measurement under deflection is necessary. And hence devices (resistors) should be designed. Meanwhile, the gauge factor measurement set up requires certain dimension of beam, which should be considered during the mask design.

5.1.1 Geometry Design Rules for Resistors

If possible, all resistors should be shaped as simple straight lines, because of their superior high-frequency performance and less likelihood of failure under humidity and load. In addition, using four wire bridge structure (Figure 5.1) to measure the resistance is more accurate because this structure excludes the contact resistance of the pad. If the width of the resistor is critical, one can also add ruler[1] parallel to the resistor. It is good for calibration in SEM, and to calculate the underetch effect. In our case, the four wire measurement structure is relatively insensitive to critical dimension loss, so there is no ruler. Still, different L- W resistors were placed in the mask. Patterns that use meandering lines and some square resistors were also included, which is good for a versatile utilization of the mask in the future.

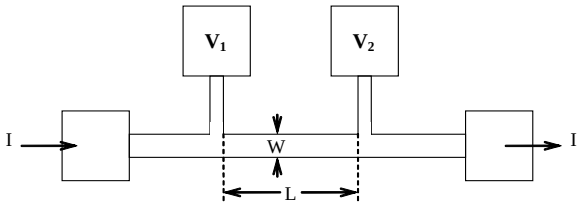

Figure 5.1: Four wire structure

5.1.2 Other Considerations during the Mask Design

Not only resistors in the direction of the beam were designed, but also resistors with a 45°, 90°, 135° angle to the beam orientation were considered during the mask design. That is because longitudinal gauge factor ($GF_{||}$) is not enough for the characterization. Perpendicular gauge factor ($GF_{\perp}$) is the fractional resistance change

[1] A test structure provides a grating of parallel structures with known lateral pitch in one or more layers, which can then be used as a build in reference for dimensional measurement[53].

to strain when the resistor is placed 90° to the beam. With the same nomenclature, angled gauge factor GF_{45^o} and GF_{135^o} can be defined.

In the upper half central area, two pairs of hall-plate like structures were placed. This is for the hall measurement without magnetic field or so called offset voltage[2].

To be convenient for the later wire bonding step, the dimensions of the bond pads were large ($300\mu m \times 300\mu m$) and they were placed as dispersed as possible in order to avoid short circuit by bonding wires touching each other.

5.1.3 The Layout

There are 8 groups of VanderPauw structures and step measurement structures on each die for testing the TCR and film thickness separately. The VanderPauw structures were designed based on the Greek cross shape and EE410 mask design from Stanford University. Base on the GF measurement set up requirement, 3 twins of beam were included in the mask design with dimension of 66.5mm long and 1.4mm wide (to fit in the grooves on carrier PCB5.2.1). To obtain differential test result, the deflected ones are mirrored along the expected dicing lines. The final layout of the mask design is as shown in Figure 5.2.

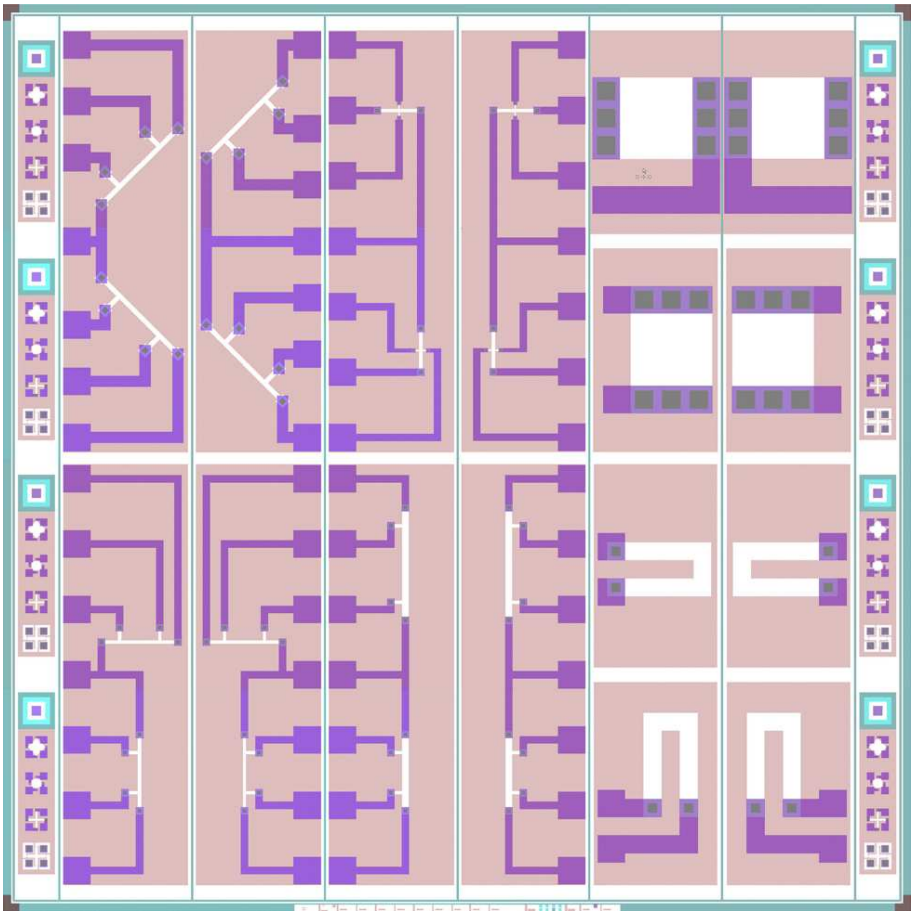

Figure 5.2: L-edit mask design layout

[2]Offset voltage (V_{os}) is a voltage produced between the output terminals of hall element when the magnetic flux density is 0. And it is one of the basic characteristics of the Hall element

5.2 Wafer Dicing, Bonding to PCB and Gauge Factor Measurement

5.2.1 PCB design

In order to use Creemer's measurement setup to do the deflection measurement, PCBs and epoxy boards are indispensable. The followings are some ideas in the design.

Printed circuit board is the bridge to connect chip electrically with peripheral interconnect (measurement equipments). Several bondable gold pads were placed on the PCB and copper traces connected those pads with DIN 41612 connector. Areas except soldering pads are covered with anti-soldering materials which gave the PCB the typical green color.

Epoxy boards are the carrier and mechanical clamping tool for silicon beams. Two grooves with the depth of $500\mu m$ were made on them. When silicon beams were placed in grooves, about $30\mu m$ of the beams emerged from epoxy board making sure that another board glued on top will provide enough force to clamp these two beams. After clamping, a 37.5mm long beam was free to be deflected.

Beam carrier glued on top of PCB with 1cm bonding pads area protruding below the epoxy. As a result, there was 1mm distance between the beam and the surface of the PCB. It is high enough for the beam deflection. More specific and detailed information can be found in Creemer's thesis [34].

Cyner Substrate helped to fabricate these PCBs after the design using Protel DXP 2004. The PCB and epoxy board are shown in Figure 5.3, and the boards with beams and a connector can be found in Figure 2.7(b).

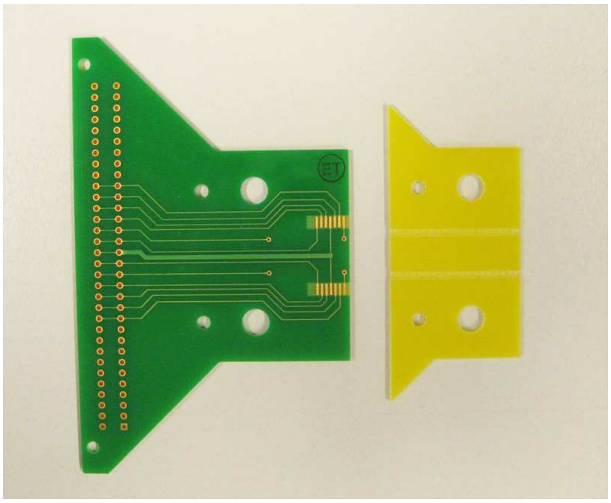

Figure 5.3: PCBs for deflection tests

5.2.2 Wafer Dicing and Wire bonding

After finishing on-chip TCR measurements, the wafers were sent to be diced into 66.5mm long and 1.4~1.5mm wide beams. Then wire-bonding step were carried out to provide the necessary electrical connections.

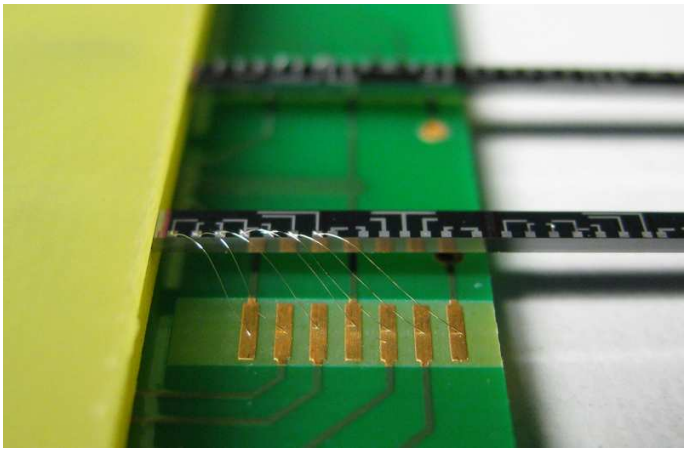

Figure 5.4: Wire bonding to PCB

5.2.3 Gauge Factor Measurement

A differential measurement was carried out to cancel the uncontrollable factors. A resistor was measured on one beam without deflection and on the other beam under external stress. By using the microscrew to adjust the position of the silicon beam tip, a deflection range from -2mm to 2mm can be achieved. This means both compressive and tensile strain effects on the resistor are measurable. If the relative resistance change v.s. strain can be fitted into a linear function, the slope is the gauge factor value.

In order to take hysteresis of gauge factor into consideration, after the beam reached the largest compressive deflection, the beam was pushed gradually back to the largest tensile deflection state and the resistance measured again.

5.2.3.1 Al-N thin films measurement results

Two aluminum nitride samples (Al-N 52 and Al-N 53) were subjected to the deflection method of longitudinal gauge factor. The fitting curve functions are provided in Figure 5.5.

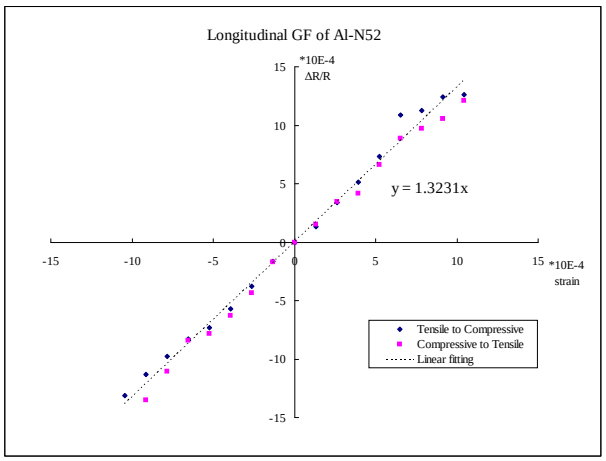

(a)

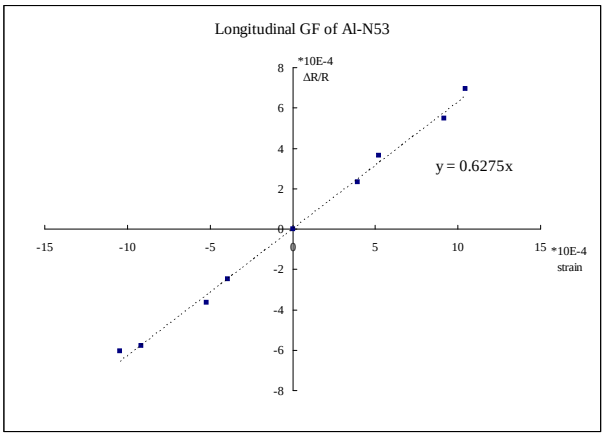

(b)

Figure 5.5: Relationship of fractional change in resistance to strain on (a)Al-N sample 52, with hysteresis test (b)Al-N sample 53. Positive strain is tensile; negative strain is compressive.

The roughness of the film and not crystallized structure lead to a relatively low gauge factor. Longitudinal gauge factor of Al-N sample 52 is 1.32 and sample 53 is only 0.6275. Although the hysteresis effect was found to be negligible in sample 52, we can conclude that our 300nm conductive Al-N thin films are not an effective piezoresistive material because of the small gauge factor.

5.2.3.2 Cr-N thin films measurement results

Chromium nitride samples have good polycrystalline structures, which ensures that they have better piezoresistive performance than Al-N layer. In addition, all the column structures are aligned along the z direction (perpendicular to the wafer surface), the piezoresistive effect should be isotropic in the x-y plane.

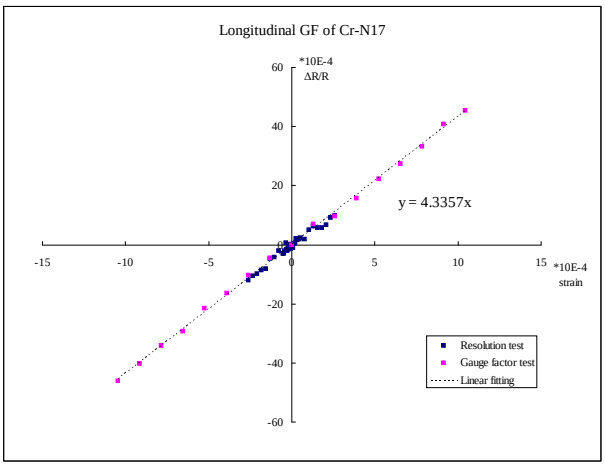

(a) Relative resistance change of longitudinal placed resistor under deflection, $GF_{||}$ =4.34.

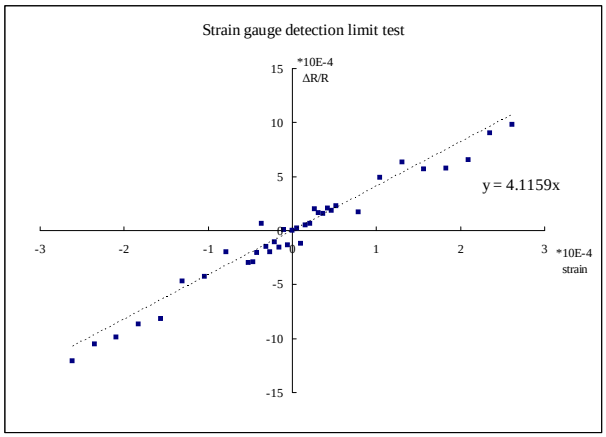

(b) Detection limit result of longitudinal placed resistor.

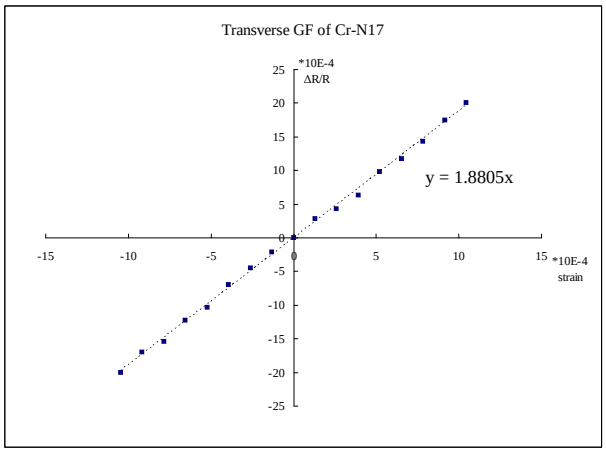

(c) Relative resistance change of perpendicular placed resistor under deflection, $GF_{\perp}$ =1.88.

Figure 5.6: Strain sensitivity test of resistors on Cr-N sample 17. Positive strain is tensile; negative strain is compressive.

In Cr-N17 sample deflection measurement, a longitudinal GF of 4.34 and a transverse GF of 1.88 were obtained (See Figure 5.6). The maximum strain of the deflection in the measurement is $\pm 1050\mu\varepsilon$ (corresponding tip displacements are $\pm 2mm$).

In order to get the resolution of the gauge resistor, resistance measurement under deflection between $\pm 0.5mm$ ($\pm 261.3\mu\varepsilon$) was carried out (See Figure 5.6(b)). The resistance change was detectable when the strain varied in step of $26.1\mu\varepsilon$ in the range of $\pm(52.3\mu\varepsilon, 1050\mu\varepsilon)$. However, when it scales down to $5.2\mu\varepsilon$ in $(-52.3\mu\varepsilon, 52.3\mu\varepsilon)$, the linear relationship becomes unclear. In conclusion, it is reliable to use this Cr-N strain resistor in the range of $\pm(52.3\mu\varepsilon, 1050\mu\varepsilon)$ and the minimum detectable strain is $26.1\mu\varepsilon$.

The sample 18' was also subjected to the longitudinal and transverse gauge factor measurement. The measurement plots are given in Figure 5.7 as follow.

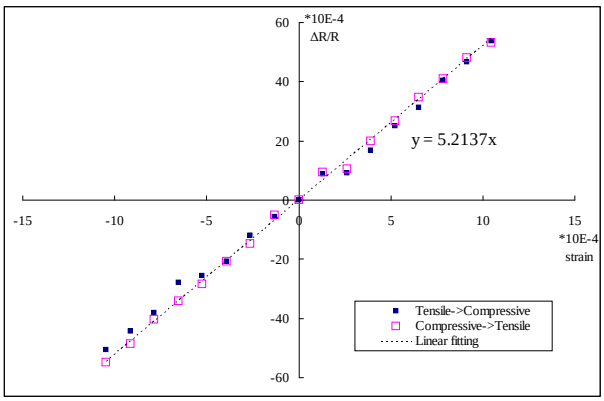

(a) Relative resistance change of longitudinal placed resistor under deflection, $GF_{||} = 5.21$.

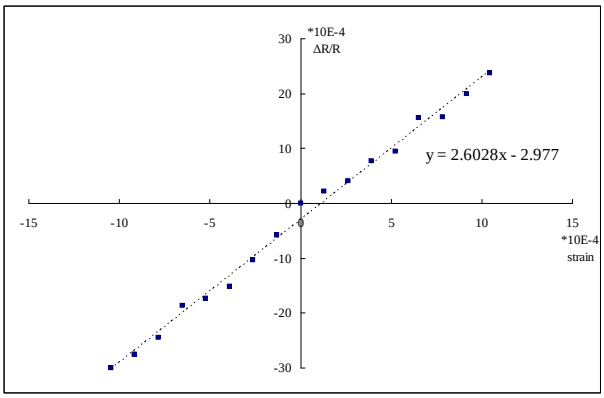

(b) Relative resistance change of perpendicular placed resistor under deflection, $GF_{\perp} = 2.60$.

Figure 5.7: Strain sensitivity test of resistors on Cr-N sample 18' . Positive strain is tensile; negative strain is compressive.

The longitudinal gauge factor of Cr-N 18' was found to be the largest (5.21) and no hysteresis effect of strain was shown in Figure 5.7(a). $GF_{\perp}$ was less than half of $GF_{||}$.

The uniformity of piezoresistive effect in x-y plane was examined as in Figure 5.8.

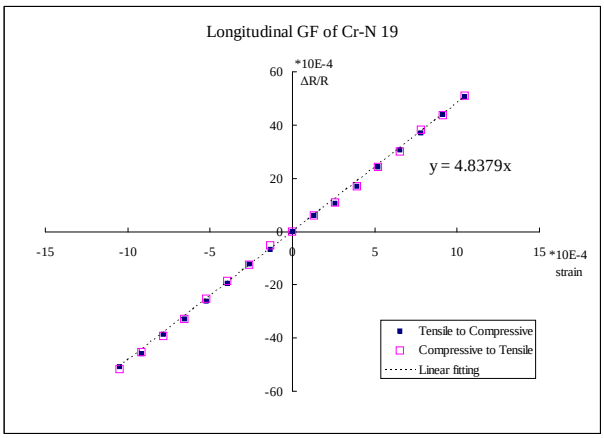

(a) Relative resistance change of longitudinal placed resistor under deflection, $GF_{||}$ =4.84, with hysteresis test.

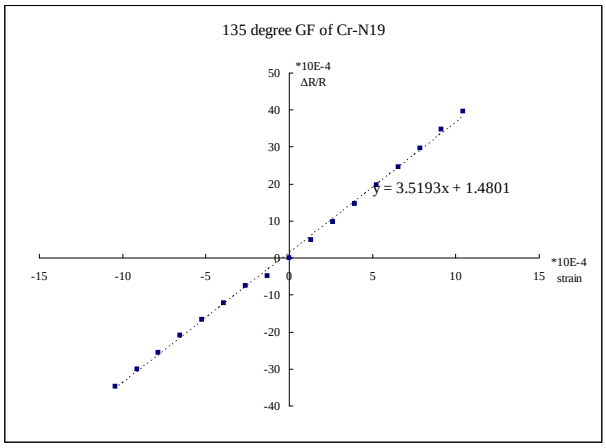

(b) Relative resistance change of 135° angled resistor under deflection, GF_{135^o} =3.52.

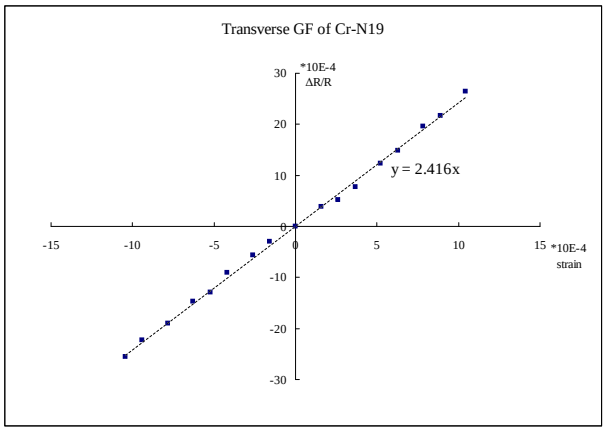

(c) Relative resistance change of perpendicular placed resistor under deflection, $GF_{\perp}$ =2.42.

Figure 5.8: Relationship of fractional change in resistance to strain on Cr-N 19. Positive strain is tensile; negative strain is compressive.

$GF_{||}$ was found to be 4.94 in sample 19 and no hysteresis effect exists (See in Figure 5.8 (a)); the moderate gauge factor value was found in the 135 angled resistor, which is 3.52; the smallest GF of Cr-N 19 is the resistor placed perpendicularly with respect to the beam.

The difference between longitudinal and transverse gauge factors can be explained from the geometry change under deflection.

Consider a block resistor, if the length of the resistor is l, the resistivity of the material is ρ, and the cross section where the current go though is $w \times t$, the resistance of the resistor is $R = \rho\left(\frac{l}{w \times t}\right)$. If the resistor is stretched longitudinally by an external force F, the stress in the block is $\sigma = F/(wt)$ and the strain (the relative elongation) in the filament is $\varepsilon = \triangle l/l = \sigma/E$, where E is the Young's Modulus of the material. Thus, the relative change in resistance caused by the force is

$$\frac{\Delta R}{R} = \frac{\Delta \rho}{\rho} + \frac{\Delta l}{l} - \frac{\Delta w}{w} - \frac{\Delta t}{t}$$

As well known in mechanics, the longitudinal stretch of block is accompanied a

lateral contraction, i.e. $\triangle w/w = \triangle t/t = -\nu\,(\triangle l/l)$, where $\Delta l > 0$, $\Delta w, \Delta t < 0$ and ν is the Poisson's ratio of the material. For most materials, ν has a value of about 0.3. Thus we have

$$\frac{\Delta R}{R} = \frac{\Delta \rho}{\rho} + \frac{\Delta l}{l}(1 + 2\nu)$$

Usually, the relative change of resistivity, $\Delta\rho/\rho$, is a function of stress/strain and is expressed as $\pi\sigma = \pi E\varepsilon$, where π is the piezoresistive coefficient of the material [8]. Therefore, we have $\Delta R/R = (\pi E + 1 + 2\nu)\,\varepsilon$, and $GF_{||} = \pi E + 1 + 2\nu \approx \pi E + 1.6$.

Likewise, if the material is isotropic in the x-y plane, when the resistor is stretched transversely (along w), $\triangle l/l = \triangle t/t = -\nu\,(\triangle w/w)$, in which $\Delta w > 0$, $\Delta l, \Delta t < 0$. The relative change in resistance is $\frac{\Delta R}{R} = \frac{\Delta \rho}{\rho} + \frac{\Delta l}{l} - \frac{\Delta w}{w} - \frac{\Delta t}{t} = \frac{\Delta \rho}{\rho} - \frac{\Delta w}{w} = (\pi E - 1)\,\varepsilon$. So the transverse gauge factor is $GF_{\perp} = \pi E - 1$.

In conclusion, for isotropic material in the x-y plane, the difference between longitudinal and transverse gauge factors is $GF_{||} - GF_{\perp} = 2.6$. From Table 5.1 we can see that the measurement data basically conform to the above calculation. This means Cr-N samples we fabricated are isotropic in the x-y plane.

Table 5.1: Longitudinal and transverse gauge factors of Cr-N samples

Sample No.	$GF_{||}$	$GF_{\perp}$	$GF_{||} - GF_{\perp}$
Cr-N 17	4.34	1.88	2.46
Cr-N 18'	5.21	2.60	2.61
Cr-N 19	4.94	2.42	2.52

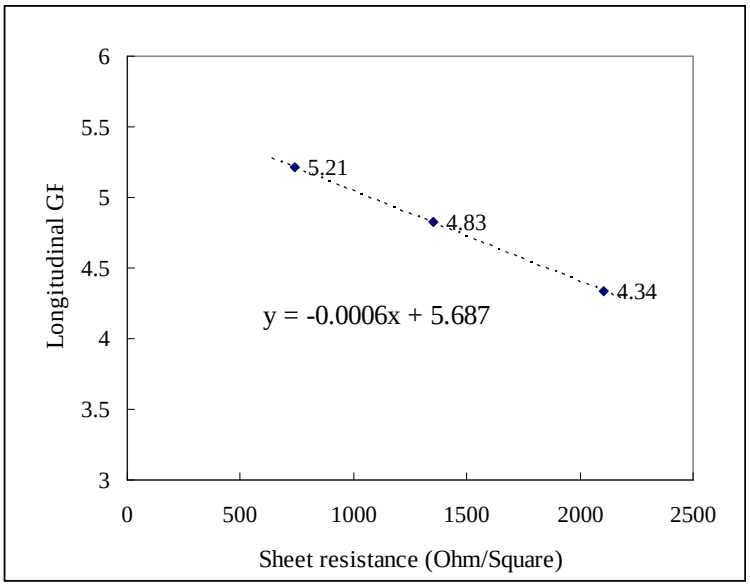

Figure 5.9: Longitudinal GF as a function of sheet resistance of the sample

The decreasing trend in GF as a function of sheet resistance is obvious in Figure 5.9. It means the largest longitudinal gauge factor will be on CrN sample 19'. The estimated value is GF=-0.0006×680.41[3]+5.687=5.47. It still needs to be verified by additional measurement.

[3]Cr-N samples sheet resistance values were listed in Table 4.9

5.2.3.3 Comments on the results

Although the above gauge factor measurement is feasible, it is worth notice that the change in voltage when the beam is under deflection is only considered to be the result of normal strain. However, in practice the shear strain caused by imperfect beam clamping is a significant source of error [34].

A change in the excitation current would also affect the reading of voltage. The accuracy of the current can be calculated from the specification of Agilent Parameter Analyzer. A current source in range of $\pm 100\mu A$ produces an inaccuracy of $\pm(0.07\%I + 40nA + 100pA \times Vout)$. Take Cr-N sample 19 under most tensile strain ($1050\mu\varepsilon$) for example. The results of sweep current and accuracy are listed in Table 5.2. We can see that the inaccuracy is less than 0.15% of the current and it could not result significant errors.

Voltage meter itself could also introduce some errors. A voltage measured in range of $\pm 2V$ possess an inaccuracy of $\pm(0.02\%V + 200\mu V)$. The calculation results are also included in Table 5.2 and the voltage inaccuracy influence could also be neglected.

Table 5.2: The inaccuracy of drive current and measured voltage

I (μA)	V1(V)	V3(V)	ΔV (V)	Current inaccuracy (μA)	Voltage inaccuracy (mV)
-50	-1.11442	-0.32080	-0.79362	±0.07499	±0.42288
-45	-1.00358	-0.28846	-0.71512	±0.07149	±0.40072
-40	-0.89188	-0.25678	-0.63510	±0.06799	±0.37838
-35	-0.78002	-0.22494	-0.55508	±0.06449	±0.35600
-30	-0.66856	-0.19216	-0.47640	±0.06100	±0.33371
-25	-0.55722	-0.16022	-0.39700	±0.05750	±0.31144
-20	-0.44586	-0.12868	-0.31718	±0.05400	±0.28917
-15	-0.33476	-0.09646	-0.23830	±0.05050	±0.26695
-10	-0.22276	-0.06372	-0.15904	±0.04700	±0.24455
-5	-0.11124	-0.03198	-0.07926	±0.04350	±0.22225
0	0.00010	0.00016	-0.00006	±0.04000	±0.20002
5	0.11144	0.03234	0.07910	±0.04350	±0.22229
10	0.22276	0.06390	0.15886	±0.04700	±0.24455
15	0.33396	0.09586	0.23810	±0.05050	±0.26679
20	0.44588	0.12870	0.31718	±0.05400	±0.28918
25	0.55768	0.16056	0.39712	±0.05750	±0.31154
30	0.66866	0.19206	0.47660	±0.06100	±0.33373
35	0.77986	0.22436	0.55550	±0.06451	±0.35597
40	0.89184	0.25714	0.63470	±0.06801	±0.37837
45	1.00330	0.28878	0.71452	±0.07151	±0.40066
50	1.11442	0.32044	0.79398	±0.07501	±0.42288

Temperature drift could happen during the test. However, the effect of any temperature dependence can be disregarded in differential measurement.

5.2.3.4 Self-heating Effect

Even though temperature variance effect can be canceled out during the differential measurement, large self-heating effect is not expected during gauge factor measure-

ment. So COMSOL Multiphysics software is introduced, which basically solves the equations involved in the Joule-heating and the thermo-electric interactions. The resistor temperature distribution when supplying $50\mu A$ current for 20ms[4] into the resistors is shown in Figure 5.10. The temperature of the resistor under test is uniformly increased for less than $1°C$. Consequently, the self-heating effect is not significant in GF measurement.

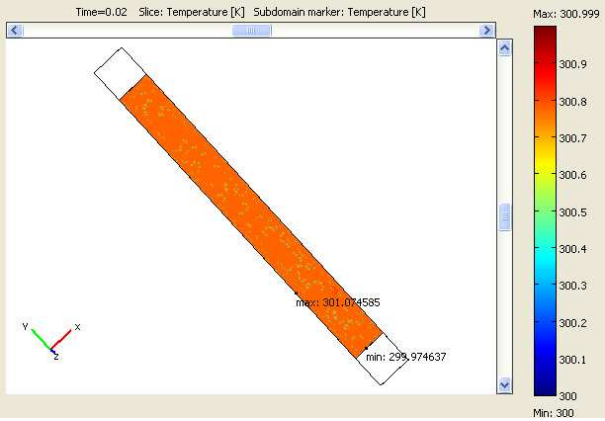

Figure 5.10: Self-heating of Cr-N 18' sample during resistance measurement

[4]Measurement integration time is 20ms.

6 Conclusions and Future Work

Thin film strain gauges are ideal strain sensors for many applications because of several advantages such as small size, minimal impact on a measured object and compatibility with IC process. Al-N and Cr-N have been reported to be potential materials for strain sensor application, however, piezoresistive properties of these two materials fabricated in low temperature haven't been well studied.

In this project, recipes of sputtering low residual stress, conductive Al-N and Cr-N thin films have been developed at first. Then resistance measurements at different temperatures revealed the temperature coefficient of resistance. Negative TCR showed semiconductor behavior for both materials and it means compensation resistors of positive TCRs will be needed in real application.

Gauge factor of these two materials has been evaluated in Chapter 5. It has been found that low resistive amorphous Al-N is less suitable for strain sensor application than Cr-N because of its insensitivity to deformation. DC magnetron reactive sputtering Cr-N exhibits uniform piezoresistive effect in x-y plane due to the column crystal structure along z direction. And the largest gauge factor of 5.21 has been found in Cr-N sample 18'. Not all devices have been measured in gauge factor yet. When finishing all the measurements, a relationship between resistivity and gauge factor could be investigated.

Further work will be done to check crystal orientation by x-ray diffraction. The expected result according to other people's work is polycrystalline chromium nitride thin films have (111) preferred crystal orientation. The dynamic deflection test can also be considered in the future, and finally the fabrication can be transferred to steel diaphragm substrate with SOG on top to check the availability for ball bearing strain sensing application.

Appendix A

TCR measurement result of different Al-N samples

Table A.1: TCR of Al-N sample 10

Die	$R_{\square}(\Omega/\square)$	$\alpha_{tcr}(\text{ppm}/^{\circ}C)$
(-3,2)	2802.86	-2728.62
(-2,1)	1853.69	-2508.74
(-1,0)	1437.02	-2411.28
(0,-1)	1435.41	-2412.92
(1,-2)	1924.45	-2535.19
(2,-3)	2819.00	-2737.53

Table A.2: TCR of Al-N sample 14

Die	$R_{\square}(\Omega/\square)$	$\alpha_{tcr}(\text{ppm}/^{\circ}C)$
(-3,2)	73.56	-521.26
(-2,1)	60.82	-721.55
(-1,0)	51.07	-693.08
(0,-1)	52.65	-704.05
(1,-2)	58.03	-733.50
(2,-3)	66.04	-787.13

Table A.3: TCR of Al-N sample 15

Die	$R_{\square}(\Omega/\square)$	$\alpha_{tcr}(\text{ppm}/^{\circ}C)$
(-3,2)	1545.80	-2289.56
(-2,1)	901.98	-1705.47
(-1,0)	286.75	-412.20
(0,-1)	414.39	-1066.87
(1,-2)	856.82	-1705.73
(2,-3)	1445.80	-2233.63

Table A.4: TCR of Al-N sample 15'

Die	$R_{\square}(\Omega/\square)$	$\alpha_{tcr}(\text{ppm}/^{\circ}C)$
(0,-4)	2333.00	-2806.69
(0,-3)	1465.86	-2431.33
(0,-2)	1258.84	-2134.50
(0,-1)	826.09	-1934.29
(0,0)	822.24	-1886.80
(0,1)	888.83	-1805.85
(0,2)	1017.35	-2093.88
(0,3)	2024.50	-2610.77

Table A.5: TCR of Al-N sample 24

Die	$R_{\square}(\Omega/\square)$	$\alpha_{tcr}(\text{ppm}/^{\circ}C)$
(0,-4)	31.56	-158.71
(0,-3)	30.04	-143.42
(0,-2)	31.43	-141.73
(0,-1)	29.03	-109.93
(0,0)	29.54	-108.53
(0,1)	28.25	-119.69
(0,2)	28.89	-140.45
(0,3)	30.41	-145.30

Table A.6: TCR of Al-N sample 24'

Die	$R_{\square}(\Omega/\square)$	$\alpha_{tcr}(\text{ppm}/^{\circ}C)$
(0,-4)	82.60	-539.98
(0,-3)	74.79	-484.02
(0,-2)	81.73	-528.60
(0,-1)	81.34	-650.35
(0,0)	91.00	-668.14
(0,1)	66.80	-443.12
(0,2)	76.02	-503.83
(0,3)	73.07	-383.20

Table A.7: TCR of Al-N sample 52

Die	$R_{\square}(\Omega/\square)$	$\alpha_{tcr}(\text{ppm}/^{\circ}C)$
(0,-4)	2516.75	-2239.50
(0,-2)	1905.86	-2066.26
(0,-1)	1744.66	-2027.73
(0,0)	1681.44	-1966.52
(0,1)	1846.86	-2009.73
(0,3)	2409.53	-2175.72

Table A.8: TCR of Al-N sample 52'

Die	$R_{\square}(\Omega/\square)$	$\alpha_{tcr}(\text{ppm}/^{\circ}C)$
(0,-4)	2930.55	-2608.04
(0,-3)	2082.26	-2101.18
(0,-2)	1773.40	-2064.17
(0,-1)	1707.54	-2168.33
(0,0)	1748.72	-2109.55
(0,1)	1729.96	-2276.47
(0,2)	1844.30	-2170.15
(0,3)	1850.55	-2003.03

Table A.9: TCR of Al-N sample 53

Die	$R_{\square}(\Omega/\square)$	$\alpha_{tcr}(\mathrm{ppm}/^{\circ}C)$
(0,-4)	47.24	-159.67
(0,-3)	48.75	-166.37
(0,-2)	50.74	-146.50
(0,-1)	53.95	-142.53
(0,0)	48.38	-156.07
(0,1)	44.62	-118.69
(0,2)	41.21	-102.89
(0,3)	43.85	-158.69

Table A.10: TCR of Al-N sample 53'

Die	$R_{\square}(\Omega/\square)$	$\alpha_{tcr}(\mathrm{ppm}/^{\circ}C)$
(0,-4)	83.42	-389.60
(0,-3)	119.51	-612.48
(0,-2)	89.78	-507.93
(0,-1)	115.33	-591.33
(0,0)	159.81	-412.99
(0,1)	138.70	-519.11
(0,2)	93.97	-439.52
(0,3)	88.43	-410.49

Table A.11: TCR of Al-N sample 55

Die	$R_{\square}(\Omega/\square)$	$\alpha_{tcr}(\mathrm{ppm}/^{\circ}C)$
(0,-4)	3372.93	-2069.83
(0,-1)	2253.89	-1524.73
(0,0)	1863.33	-1299.47
(0,1)	1747.86	-1080.24

B-parameter curve fitting result of different Cr-N samples

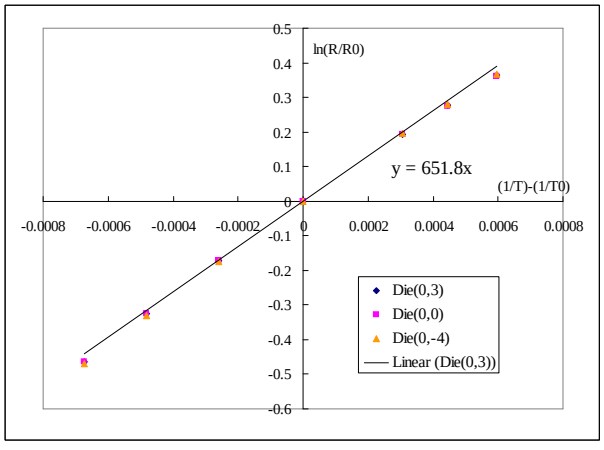

Figure A.1: Cr-N sample 18

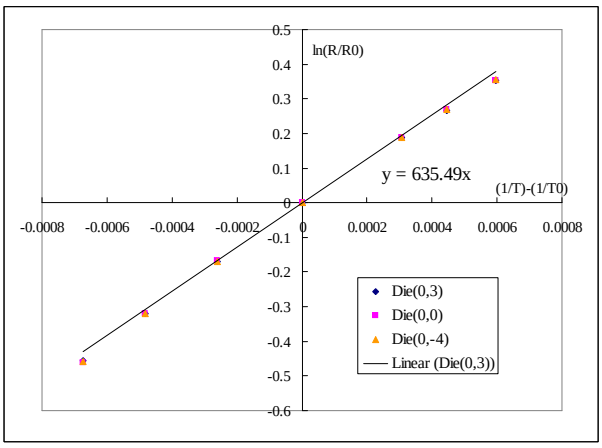

Figure A.2: Cr-N sample 19

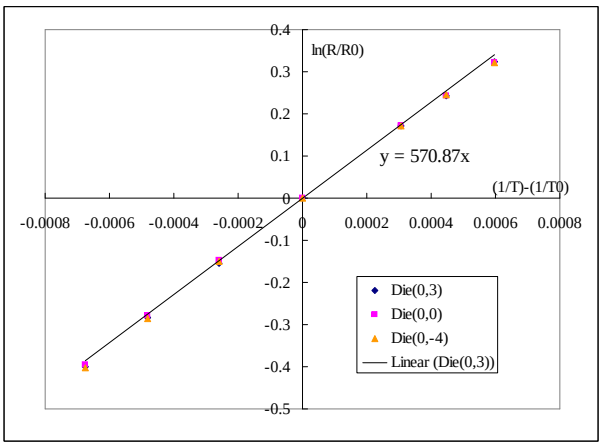

Figure A.3: Cr-N sample 18'

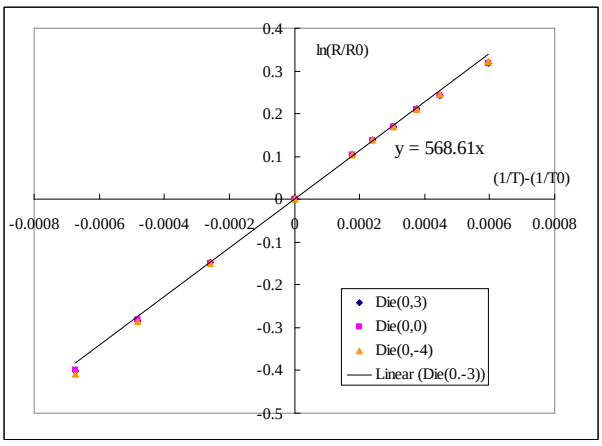

Figure A.4: Cr-N sample 19'

Appendix B

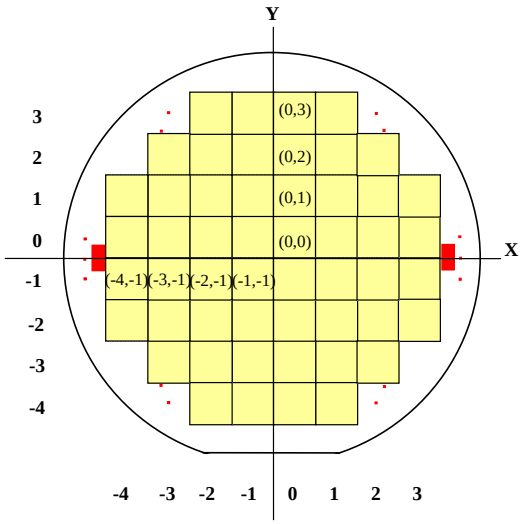

Figure B.1 Coordinates on wafer

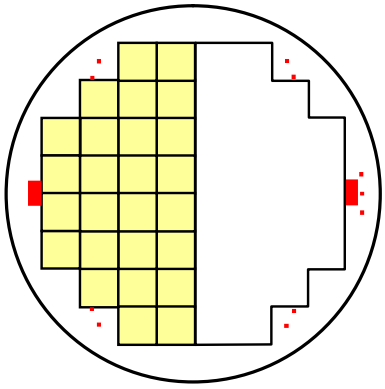

Figure B.2 Half wafer patterning sketch (yellow color area are patterned)

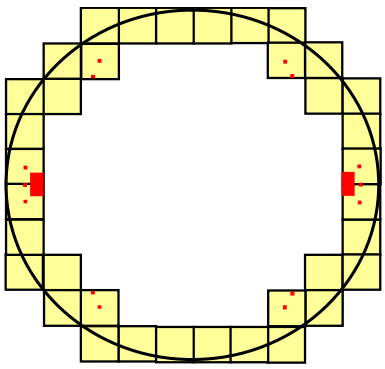

Figure B.3 Exposure area in lithography job “g10a-edge(full): ID2”

Acknowledgment

Here I want to express my gratitude to all the people who helped me with my master thesis.

I would like to thank Prof. dr. P.M. Sarro for introducing me to the Laboratory ECTM. I would like to thank Henk Mol from SKF Company for providing me this great opportunity to be engaged in this interesting and exploratory project.

I would like to express my appreciation to Hugo Schellevis. I can not accomplish this work without his generous assistance, patient guidance and valuable suggestions.

I am thankful to Dr. Fredrik Creemer. I really benefit from his previous study about piezojunction effect and his delicate beam deflection test setup.

I would also like to thank Peter Swart for his great help in measurement room. Big thanks to Loek Steenweg and Wim van der Vlist for wafer dicing and wire-bonding.

I am grateful that An Tran is always available for helping me do wet etching step in AlN fabrication.

Thanks for Johan van der Cingel, Silvana Milosavljević, Charles de Boer and Mario Laros for training me to be a qualified trainee working in Dimes cleanroom. To DIMES ICP group, I'd like to thank them for their kind help in cleanroom.

My appreciation also extents to: Shuoxi Chen, Fabio Santagata, Luigi Mele, Luigi La Spina, Sten Vollebregt, Gianpaolo Lorito and all the other colleagues and staffs in DIMES.

Bibliography

[1] T. Nagayama, M. Ruiz-s, B.F. Spencer, K.A. Mechitov, and G. Agha. Wireless strain sensor development for civil infrastructure. In *Proc., 1st Int. Workshop on Networked Sensing Systems*, pages 97–100, 2004.

[2] L.J. Boudreaux and J.H. Foster. Thin film strain gauge and method of fabrication, August 1978.

[3] J.W. Dally and W.F. Riley. *Experimental Stress Analysis*. McGraw-Hill, 3rd edition, 1991.

[4] C.S. Smith. Piezoresistance effect in germanium and silicon. *Physical Review*, 94(1):42–49, Apr 1954.

[5] S.C. Kim and K.D. Wise. Temperature sensitivity in silicon piezoresistive pressure transducers. *IEEE Transactions on Electron Devices*, 30(7):802 – 810, jul 1983.

[6] S. Neumann. High temperature pressure sensor based on thin film strain gauges on stainless steel for continuous cylinder pressure control. In *CIMAC Conference, Mai 2001*, 2001.

[7] S. Kon, K. Oldham, and R. Horowitz. Piezoresistive and piezoelectric MEMS strain sensors for vibration detection. *Proceedings of SPIE - The International Society for Optical Engineering*, 6529:65292V–1 – 65292V–11, 2007.

[8] M. Bao. *Analysis and Design Principles of MEMS Devices*. Elsevier Science, first edition edition, June 2005.

[9] O.J. Gregory, A.B. Slot, P.S. Amons, and E.E. Crisman. High temperature strain gages based on reactively sputtered AlN_x thin films. *Surface and Coatings Technology*, 88(1-3):79 – 89, 1997.

[10] http://www.matweb.com/search/datasheet.aspx?matguid=ffbf753c500949db95e502e043f9a404.

[11] J.-F. Lei, H. Okimura, and J.O. Brittain. Evaluation of some thin film transition metal compounds for high temperature resistance strain gauge application. *Materials Science and Engineering: A*, 111:145 – 154, 1989.

[12] G.C.A.M. Janssen, F.D. Tichelaar, and C.C.G. Visser. Stress gradients in CrN coatings. *Journal of Applied Physics*, 100(9):093512, 2006.

[13] G.S. Chung, W.J. Lee, and J.S. Song. Characteristics of chromium nitride thin-film strain gauges. *Sensors and Materials*, 13:13 – 21, 2001.

[14] R. Djugum, E.C. Harvey, and E.D. Doyle. A fabrication process for CrN/TiAlN multi-layered strain gauges on mild steel. *Journal of Micromechanics and Microengineering*, 16(8):1475, 2006.

[15] R. Djugum. *Novel Fabrication Processes for Thin Film Vapour Deposited Strain Gauges on Mild Steel.* PhD thesis, School of Engineering and Science, Swinburne University of Technology, Australia, 2006.

[16] H. Yamadera and Y. Taga. Cr-O-X film as a strain gauge. *Thin Solid Films*, 206(1-2):107 – 110, 1991.

[17] G.S. Chung. Characteristics of tantalum nitride thin film strain gauges for harsh environments. *Sensors and Actuators A: Physical*, 135(2):355 – 359, 2007.

[18] C.M. Wang, J.H. Hsieh, and C. Li. Electrical and piezoresistive properties of TaN-Cu nanocomposite thin films. *Thin Solid Films*, 469-470:455 – 459, 2004.

[19] I. Ayerdi, E. Castano, A. Garcia-Alonso, and F.J. Garcia. Characterization of tantalum oxynitride thin films as high-temperature strain gauges. *Sensors and Actuators A: Physical*, 46(1-3):218 – 221, 1995.

[20] G. Schultes, M. Schmitt, D. Goettel, and O. Freitag-Weber. Strain sensitivity of TiB_2, $TiSi_2$, $TaSi_2$ and WSi_2 thin films as possible candidates for high temperature strain gauges. *Sensors and Actuators A: Physical*, 126(2):287 – 291, 2006.

[21] O.J. Gregory, T. You, and E.E. Crisman. Effect of aluminum doping on the high-temperature stability and piezoresistive response of indium tin oxide strain sensors. *Thin Solid Films*, 476(2):344 – 351, 2005.

[22] L.J. van der Pauw. A method of measuring specific resistivity and hall effect of disc of arbitrary shape. *Philips Research Reports*, 13:1 – 9, 1958.

[23] T. Fischer. *Materials Science for Engineering Students.* Elsevier Inc., 2009.

[24] Alvaro Artieda, Michela Barbieri, Cosmin Silviu Sandu, and Paul Muralt. Effect of substrate roughness on c-oriented aln thin films. *Journal of Applied Physics*, 105(2):024504, 2009.

[25] S.H.N. Lim, D.G. McCulloch, M.M.M. Bilek, and D.R. McKenzie. Relation between microstructure and stress in titanium nitride films grown by plasma immersion ion implantation. *Journal of Applied Physics*, 93(7):4283–4288, 2003.

[26] D. Neamen. *Semiconductor Physics And Devices.* McGraw-Hill, 3rd edition edition, 2002.

[27] S.M. Sze. *Semiconductor Devices: Physics and Technology.* Wiley, 2nd edition, 2001.

[28] J.S. Steinhart and S.R. Hart. Calibration curves for thermistors. *Deep Sea Research and Oceanographic Abstracts*, 15(4):497 – 503, 1968.

[29] O.J. Gregory and Q. Luo. A self-compensated ceramic strain gage for use at elevated temperatures. *Sensors and Actuators A: Physical*, 88(3):234 – 240, 2001.

[30] A.L. Window and G.S. Holister. *Strain Gauge Technology.* Applied Science Publisher, 1982.

[31] H. Chiriac, M. Urse, F. Rusu, C. Hison, and M. Neagu. Ni-ag thin films as strain-sensitive materials for piezoresistive sensors. *Sensors and Actuators A: Physical*, 76(1-3):376 – 380, 1999.

[32] K.I. Arshak, F. Ansari, D. Collins, and R. Perrem. Characterisation of a thin-film/thick-film strain gauge sensor on stainless steel. *Materials Science and Engineering: B*, 26(1):13 – 17, 1994.

[33] J. Engel, J. Chen, and C. Liu. Strain sensitivity enhancement of thin metal film strain gauges on polymer microscale structures. *Applied Physics Letters*, 89(22):221907, 2006.

[34] J.F. Creemer. *The Effect of Mechanical Stress on Bipolar Transistor Characteristics*. PhD thesis, Technische Univesiteit Delft, 2002.

[35] R. Mateiu, M. Lillemose, T.S. Hansen, A. Boisen, and O. Geschke. Reliability of poly 3,4-ethylenedioxythiophene strain gauge. *Microelectronic Engineering*, 84(5-8):1270 – 1273, 2007. Proceedings of the 32nd International Conference on Micro- and Nano-Engineering.

[36] J.K. Kim, C.S. Park, D.W. Lee, S.M. Cho, and C.R. Han. Measurement of the gauge factor of carbon fiber and its application to sensors. *Microelectronic Engineering*, 85(5-6):787 – 791, 2008. Proceedings of the Micro- and Nano-Engineering 2007 Conference - MNE 2007.

[37] Standard test methods for performance characteristics of metallic bonded resistance strain gauges, 2009. Organization of International Legal Metrology.

[38] F. Vacandio, Y. Massiani, P. Gravier, and A. Garnier. A study of the physical properties and electrochemical behaviour of aluminium nitride films. *Surface and Coatings Technology*, 92(3):221 – 229, 1997.

[39] T. Nakano and S. Baba. Gas pressure effects on thickness uniformity and circumvented deposition during sputter deposition process. *Vacuum*, 80(7):647 – 649, 2006.

[40] L.I. Maissel, R. Glang, and et al. *Handbook of Thin Film Technology*. McGraw-Hill, 1970.

[41] C. Nouveau, M.A. Djouadi, O. Banakh, R. Sanjines, and F. Levy. Stress and structure profiles for chromium nitride coatings deposited by r.f. magnetron sputtering. *Thin Solid Films*, 398-399:490 – 495, 2001.

[42] L. Chekour, C. Nouveau, A. Chala, C. Labidi, N. Rouag, and M.A. Djouadi. Growth mechanism for chromium nitride films deposited by magnetron and triode sputtering methods. *Surface and Coatings Technology*, 200(1-4):241 – 244, 2005.

[43] H.C. Barshilia, N. Selvakumar, B. Deepthi, and K.S. Rajam. A comparative study of reactive direct current magnetron sputtered CrAlN and CrN coatings. *Surface and Coatings Technology*, 201(6):2193 – 2201, 2006.

[44] T. Elangovan, P. Kuppusami, R. Thirumurugesan, V. Ganesan, E. Mohandas, and D. Mangalaraj. Nanostructured CrN thin films prepared by reactive pulsed DC magnetron sputtering. *Materials Science and Engineering: B*, 167(1):17 – 25, 2010.

[45] Y. Tsuchiya, K. Kosuge, Y. Ikeda, T. Shigematsu, S. Yamaguchi, and N. Nakayama. Non-stoichiometry and antiferromagnetic phase transition of NaCl-type CrN thin films prepared by reactive sputtering. *Materials Transactions*, 37(2):121–129, 1996.

[46] D. Gall, C.-S. Shin, R.T. Haasch, I. Petrov, and J.E. Greene. Band gap in epitaxial NaCl-structure CrN(001) layers. *Journal of Applied Physics*, 91(9):5882–5886, 2002.

[47] E. Martinez, R. Sanjines, O. Banakh, and F. Levy. Electrical, optical and mechanical properties of sputtered CrN_y and $Cr_{1-x}Si_xN_{1.02}$ thin films. *Thin Solid Films*, 447 - 448:332 – 336, 2004.

[48] B. Bhushan and B.K. Gupta. *Handbook of tribology*. McGraw-Hill, 1991. p. 4.54.

[49] S. Inoue, F. Okada, and K. Koterazawa. CrN films deposited by rf reactive sputtering using a plasma emission monitoring control. *Vacuum*, 66(3-4):227 – 231, 2002.

[50] Y. Iba, F. Kumasaka, H. Aoyama, T. Taguchi, and M. Yamabe. Pattern etching of Ta X-ray mask absorber on SiC membrane by inductively coupled plasma. *Japanese Journal of Applied Physics*, 37(Part 2, No. 7A):L824–L826, 1998.

[51] R. Mientus, R. Grotschel, and K. Ellmer. Optical and electronic properties of CrO_xN_y films, deposited by reactive dc magnetron sputtering in $Ar/N_2/O_2(N_2O)$ atmospheres. *Surface and Coatings Technology*, 200(1-4):341 – 345, 2005. PSE 2004.

[52] Costel Constantin, Muhammad B. Haider, David Ingram, and Arthur R. Smith. Metal/semiconductor phase transition in chromium nitride(001) grown by rf-plasma-assisted molecular-beam epitaxy. *Applied Physics Letters*, 85(26):6371–6373, 2004.

[53] K.-J. Chang, R.G. Mathews, S.A. Chou, and A. Dubey. Method for determining on-chip sheet resistivity, 2002.